JOURNAL OF GEOPHYSICAL RESEARCH, VOL. ???, XXXX, DOI:10.1002/,

Bottom-slope-induced net sheet-flow sediment transport rate under sinusoidal oscillatory flows

Jing Yuan[1], Zhiwei Li[1], O. S. Madsen[2]

[1]Department of Civil and Environmental Engineering, National University of Singapore, Singapore

[2]R.M. Parsons Laboratory, Department of Civil and Environmental Engineering, Massachusetts Institute of Technology, Cambridge, Massachusetts, USA.

Key Points.

(Type in Key Points Here)

Abstract. It is generally believed that the slope of beaches can lead to a net downslope (usually offshore) sediment transport rate under shoaling waves, but very few high-quality measurements have been reported for a quantitative understanding of this phenomenon. In this study, full-scale (1:1) experiments of bottom-slope-induced net sheet-flow sediment transport rate under sinusoidal oscillatory flows are conducted using a tilting oscillatory water tunnel. The tests cover a variety of flow-sediment conditions on bottom slopes up to 2.6°. A laser-based bottom profiler system is developed for measuring net transport rate based on the principle of mass conservation. Experimental results suggest that for a given flow-sediment condition the net transport rate is in the downslope direction and increases linearly with bottom slope. A conceptual model is presented based on the idea that gravity helps bottom shear stress drive bedload transport and consequently enhances (reduces) bedload transport and suspension when the flow is in the downslope (up-slope) direction. The model predicts both the measured net sediment transport rates and the experimental linear relationship between net transport rates and bottom slope with an accuracy generally better than a factor of 2. Some measured net transport rates in this study are comparable to those due to flow skewness obtained in similar sheet-flow studies, despite that our maximum slope could be milder than the actual bottom slope in surf zones, where sheet-flow conditions usually occur. This shows that the

slope effect may be as important as wave nonlinearity in producing net cross-shore sheet-flow sediment transport.

1. Introduction

In the coastal environment shoaling waves are the major drivers for sediment transport in the cross-shore direction, which is critical for understanding morphological evolution of beach profiles. Wave boundary layers are usually approximated by sinusoidal oscillatory flows with symmetric half-periods, so on a horizontal bottom a zero net cross-shore sediment transport (CSST) should always be expected. Thus, a net CSST must be due to some secondary factors that can induce a slight imbalance between the onshore and offshore half-periods.

Virtually all previous studies focused on the sheet-flow regime, i.e. under very intense flow conditions sediment transport takes place in a thin layer (the sheet-flow layer) above a dynamically flat movable bed. Two factors for net CSST under sheet-flow conditions have been extensively studied in the past: wave nonlinearity and cross-shore current. As waves propagate into shallow waters, their nonlinear features become significant and the associated oscillatory boundary layer flows exhibit asymmetry and skewness between the two half-periods. There are many studies focused on the effects of flow asymmetry and skewness on boundary layer flows [e.g. *van der A et al.*, 2011; *Gonzalez-Rodriguez and Madsen*, 2011; *Yuan and Madsen*, 2014] and sediment transport [e.g. *Ribberink and Al-Salem*, 1995; *Gonzalez-Rodriguez and Madsen*, 2007; *van der A et al.*, 2010]. Generally speaking, wave nonlinearity makes the flow during the onshore half-period stronger than that during the offshore half-period, so a net onshore CSST is produced. However, detailed intra-wave measurements of velocities and suspended sediment concentrations [e.g. *van der Werf et al.*, 2007; *Ruessink et al.*, 2011] also suggest that for fine sands the phase lag between sediment suspension and flow velocity can lead to a net offshore transport rate. In the coastal region, an offshore current (undertow) is established to balance the wave-associated onshore mass transport above the wave troughs, so the current-related net CSST is usually in the offshore direction. However, boundary layer streaming produced by wave propagation [e.g. *Longuet-Higgins*, 1953] and wave nonlinearity [e.g. *Trowbridge and Madsen*, 1984] can also significantly affect offshore currents and net CSST. Wave-current boundary layer flows have been extensively studied [e.g. *Grant and Madsen*, 1979; *Davies et al.*, 1988; *Holmedal et al.*, 2003], and some experimental results on net sediment transport rate under collinear wave-current flows have been reported, e.g. *Mclean et al.* [2001] for currents plus sinusoidal oscillatory flows and *Dong et al.* [2013] for currents plus skewed oscillatory flows.

The sea bottom in coastal regions usually has a mild slope with the downslope direction being offshore. The gravity force parallel to the bottom reduces the critical bottom shear stress for the threshold of sediment motion and enhances the flow's ability to transport sediment in the downslope (offshore) direction. The opposite situation occurs in the upslope (onshore) direction, so a net downslope (offshore) transport rate is produced. Thus, besides wave nonlinearity and cross-shore current, bottom slope is another secondary factor producing a net CSST. There are very few experimental studies focused on this topic, possibly because it is impossible to isolate the bottom-slope effect from the effects of wave nonlinearity and cross-shore current in wave flumes or wave tanks, since they will always co-exist when surface waves are propagating over a sloping bottom. This problem can be avoided if experiments are conducted using oscillatory water tunnels (OWT). These facilities are usually U-shaped tunnels with a piston located at one end of the tunnel generating uniform oscillatory flows. If the facility can be tilted, it can produce purely sinusoidal oscillatory flows on a sloping bottom, so the obtained net transport rate is solely due to the effect of bottom slope. *King* [1991] in his OWT study measured the average sediment transport rate under a half-period of sinusoidal flow on a sloping bottom. His experimental results showed that bottom slope increases (decreases) the half-period transport rate in the downslope (upslope) direction, so a net downslope transport rate under a full sinusoidal flow can be expected. However, approximating a sinusoidal flow by two separated half-period flows potentially distorts periodic unsteady effects. Furthermore, sediment suspension may not have sufficient time to reach the equilibrium state during a half-period. Thus, his experimental results may not be quantitatively reliable. It should also be noted that most of his experiments are not within the sheet-flow regime, so the results are not directly relevant to sheet-flow conditions. To the authors' knowledge, there are no similar OWT studies reported in the literature, so we do not have enough experimental evidence to assess the importance of bottom-slope effect on the net sheet-flow CSST.

Understanding the detailed physics of sheet-flow sediment transport requires a phase-resolving model that can predict the unsteady intra-period variation of boundary layer flow and sediment transport. There are two major approaches for developing such models: the single-phase and the two-phase approaches. The two-phase approach is based on the multi-phase-flow theory, whereby the conservation principles of mass and momentum for both fluid and sediment phases are modeled separately, including the mutual interactions between phases. This approach can in principle provide a direct simulation of the sheet-flow layer, e.g. the suspension of sediments from the seabed can be directly predicted. Existing two-phase models differ in their choices of turbulence-closure model, e.g. mixing-length theory [e.g. *Asano*, 1992], one-equation [e.g. *Li et al.*, 2008] and two-equation closures [e.g. *Amoudry et al.*, 2008]. Closure models are also required for the interactions between the two phases and the stress terms that arise from the averaging process for both phases. Therefore, model performance depends heavily on the chosen closure models, especially the turbulence-closure model [see *Amoudry*, 2012]. The single-phase approach adopts the conventional way to predict sediment transport, i.e. splitting the total sediment transport into bedload and suspended-load. The suspended sediment particles are assumed to move with the fluid, except for the settling velocity, so sediment suspension is predicted by solving the turbulent-diffusion equation with an empirical bottom boundary condition, e.g. a reference concentration. This approach is at a lower level of complexity than the two-phase approach, so it requires much less computational resources. Nevertheless, the key physics for net sheet-flow sediment transport rate can still be captured for a variety of flow-sediment conditions, so single-phase models have been successfully applied to predict the net sheet-flow sediment transport rate due to boundary layer streaming [e.g. *Kranenburg et al.*, 2013; *Fuhrman et al.*, 2013] and flow asymmetry (velocity and acceleration skewness) [e.g. *Ruessink et al.*, 2009]. Since sheet flows occur in the close vicinity of the seabed, some studies assume that bedload transport dominates. This may not be true for fine-sand scenarios (diameter$\sim$ 0.1mm), because the fine particles can be suspended further up into the water column, and the phase-lag effect becomes important, i.e. the suspended fine particles cannot immediately settle down to the sand bed at the moment of flow reversal, which can even lead to a net suspended-load transport opposing the net bedload transport. The suspension effect becomes increasingly significant with the ratio, u_{*m}/w_f, where w_f is the sediment settling velocity and u_{*m} is the maximum shear velocity within a wave period, which represents the flow's ability to suspend sediments. *Gonzalez-Rodriguez and Madsen* [2007] developed a conceptual model for net bedload transport rate under sheet-flow conditions. In this model, the intra-period variation of bedload transport rate is predicted with the instantaneous bottom shear stress and the bedload formula proposed by *Madsen* [1991]. For cases with $u_{*m}/w_f < 2.7$, including some sheet-flow experiments under velocity-skewed waves (see their figure 9) and some half-period experiments (not within the sheet-flow regime) by *King* [1991] (see their figure 7), the predictions are in good agreement with the measurements. This demonstrates the predictive ability of the bedload formula proposed by *Madsen* [1991], and also shows that it is appropriate to conceptualize sheet-flows as bedload for $u_{*m}/w_f < 2.7$. However, for cases with $u_{*m}/w_f > 2.7$ (mostly fine-sand scenarios) the model performance is very poor (see their figures 7 and 12), indicating that the suspended-load becomes dominant. Therefore, a single-phase model for sheet-flow conditions must include both bedload and suspended-load components.

There are very few theoretical studies on bottom-slope-induced net sheet-flow sediment transport rate. *Madsen* [2002] presented a simple analytical formula for bottom-slope-induced net bedload transport rate for small slopes and strong wave conditions. Without reliable measurements, the validity of this theoretical model cannot be ascertained.

In this paper we present an OWT study of bottom-slope-induced net sediment transport rate in the sheet-flow regime, as well as a conceptual model, which includes a bedload module following the approach adopted by *Gonzalez-Rodriguez and Madsen* [2007] and a new suspended-load module. The outline of this paper is as follows. In section 2 we present the experimental facility. Experimental conditions and data analysis methodology are discussed in section 3. Experimental results are presented in section 4. The conceptual model is presented and validated against experimental results in section 5. Conclusions are provided in section 6.

2. Experimental facility

2.1. Wave-Current-Sediment facility

In this study full-scale (1:1) experiments are conducted in the Wave-Current-Sediment (WCS) facility in the Hydraulic Engineering Lab of the Civil and Environmental Engineering Department at the National University of Singapore. The main part of the WCS is a 10 m-long, 50 cm-deep and 40 cm-wide enclosed test section with transparent sidewalls and lids along its entire length. A 20 cm-deep and 9 m-long trough in the test section is designed for holding sediments. Oscillatory flows are generated by a hydraulically-driven piston located in one of the two cylindrical 1 m-diameter risers attached to the two ends of the test section. The maximum flow velocity and acceleration in the test section are about 2 m/s and 2 m/s^2, which are sufficiently high to create sheet-flow conditions. *Yuan and Madsen* [2014] showed that the system can very precisely generate the specified piston motion and the cross-sectional average velocity predicted from the piston velocity is in excellent agreement with the actual free-stream velocity measured in the test section. The overall inaccuracy in generating the intended free-stream oscillatory flow in the WCS is assessed to be less than 1 cm/s, which is immaterial compared to the amplitudes of oscillatory flows in this study (O(100 cm/s)), so it is not necessary to verify the free-stream flow with velocity measurements.

The entire facility is supported by a pivot and a hydraulic jack, so it can be tilted to give a bottom slope up to approximately 2.60° or 1/22. The tilting of the WCS can be controlled with 0.01° accuracy by reading a digital slope meter mounted on the WCS, so the bottom slope β can be obtained as

$$\beta = \beta_0 + \Delta\beta \tag{1}$$

where β_0 is the actual slope of the WCS with the slope meter's reading being 0.00°. To determine β_0, we filled water into the test section with a flat movable bed, and used the water depth difference (about 15 mm) between the two ends of the test section (9 m apart) to get $\beta_0 \approx 0.10°$.

2.2. Laser-based Bottom Profiler system

As will be elaborated in section 3.3, the net sediment transport rate in the WCS is obtained based on the principle of sediment-volume conservation, which requires the measurements of bottom profile change Δz, so a Laser-based Bottom Profiler (LBP) system is developed to accurately measure Δz. The general concept of the LBP system is illustrated in Figure 1a. Several laser-sheet units mounted above the test section introduce vertical red laser sheets into the test section through the transparent lids, creating a continuous laser line on the movable bed in the test section's longitudinal direction. Digital cameras capture images of the laser line in a dark environment through the large sidewall viewing windows, so the images show red laser lines on a black background, which can be used to locate the laser line. By comparing images before ($t = t_0$) and after ($t = t_1$) a test, the vertical displacement of the laser lines, $\Delta Z(X)$, is obtained in pixels (see Figure 1b), where X is the longitudinal image coordinate ($X = 0$ is at image's left edge). With predetermined calibration parameters $\Delta Z(X) = Z(x, t_1) - Z(x, t_0)$ can be translated into a longitudinal profile of bottom elevation change $\Delta z(x)$ in millimeters, where x is the longitudinal coordinate of the test section. Since some variation of $\Delta z(x)$ across the width of the channel is inevitable, we produce two continuous laser lines located symmetrically around the lateral centerline. The average of the two profiles is taken as the final measurement.

To produce two laser lines covering the 9 m-long test section, 24 laser units, each covering a 75-cm segment of bottom, are carefully positioned and mounted on two laser support beams placed on top of the truss carrying the WCS (Figure 1c). Each unit's actual coverage is a bit longer than 75 cm to allow a 1-4 cm overlap between adjacent laser-line segments. Six Nikon D5200 cameras (resolution 6000-by-4000 pixels) are carefully mounted with a uniform 150($\pm$0.1) cm spacing on a camera support beam (CSB) parallel to the WCS, so each camera will cover a 150-cm part of the test section (Figure 1c). The CSB is located about 100 cm horizontally and 70 cm vertically from the lateral centerline of the movable bed, leading to a roughly 30° viewing angle for the cameras.

The raw digital images are first rectified and enhanced using Adobe Photoshop CS6 to remove perspective distortions and any significant ambient noise on the black image background. The laser line on a digital image is a red band (20 to 40 pixels wide) with the digital redness value (from 0 to 255 with 0 being black and 255 being red) across the red band decaying toward the edges in a manner resembling a normal distribution. Following *Yuan and Madsen* [2014], we perform normal-distribution fitting to the cross-band redness variation for each X-location and take the fitted peak as the position of the laser line $Z(X)$ (in pixels). Based on some targets with known dimensions drawn on the front sidewall of the WCS, we first obtain the horizontal and vertical calibration parameters for the vertical plane of the WCS' front sidewall. We then translate them into those for the vertical planes of the two laser lines using pre-calibrated empirical formulas. For each camera the region outside its intended coverage, i.e. 150 cm (or ±75 cm horizontally from the image's vertical centerline), is removed, and the remaining measurements are combined to give the 9-m-long longitudinal profile of $\Delta z(x)$ over the entire movable bed.

A preliminary test was conducted to test the accuracy of the LBP system. In this test, the bottom profile change of an untouched sand bed, which should be zero everywhere, was measured with the LBP. The obtained Δz is essentially a random noise with a standard deviation of $O(0.1\text{ mm})$ and a zero mean value. This suggests that the LBP is able to measure bottom profile changes with a 0.1 mm inaccuracy, which is comparable to the diameter of fine sands used in this study. In another preliminary test, an artificial bottom profile change was produced by gluing "ripples" with known geometry (plastic shells cut from circular pipes) onto a flat bottom, and the LBP accurately obtained this bottom profile change with a 0.1 mm inaccuracy.

The transparent lids of the WCS allow us to apply the LBP without removing the lids, so we are able to measure bottom profile change even during an ongoing experiment, except when sediment suspension is so significant that the laser sheets cannot reach the bottom. This feature, although not used in this study, is a key advantage of the LBP, since it allows continuous measurements of bedform development in the test section. The CSB is pivoted co-axially with the WCS, and both are equipped with slope meters with an accuracy of 0.01°, so the CSB and the WCS can be tilted in unison, enabling easy use of the LBP for a sloping WCS.

3. Experimental conditions and data analysis methodology

3.1. Sediment characteristics

Three types of well-sorted sands are used in this study, and they are referred to as fine ($d_{50} = 0.13$mm), medium ($d_{50} = 0.24$mm), and coarse ($d_{50} = 0.51$mm) sands hereafter. Their characteristics are summarized in Table 1. The sediment diameter and particle-size distribution are obtained using the Mastersizer 2000 laser particle analyzer. The uniformity of sediment particle composition is characterized by the geometric standard deviation

$$\sigma_g = \frac{1}{2}(\frac{d_{84}}{d_{50}} + \frac{d_{50}}{d_{16}}) \quad (2)$$

where d_{84} and d_{16} are particle diameters for which 84% and 16%, respectively, of the sediment sample are finer. The obtained σ_g is less than 1.5 (Table 1), and is comparable to the values of well-sorted sands used in similar studies [e.g. *O'Donoghue and Wright*, 2004]. The specific density, s, of the sands is measured using the density-bottle method. The obtained values are very close to the standard value, 2.65, used in engineering practice, and their standard deviation is less than 1% of the average values (Table 1).

We carefully fill the 20 cm-deep trough of the test section with sand to create a 20 cm-thick and 9 m-long movable bed in the WCS. Before most tests, the movable bed is flattened underwater using an aluminum scraper, so its surface layer is disturbed, and should have a porosity close to the maximum underwater porosity, ϵ_m, associated with the loosest underwater compaction. Since it is difficult to obtain in-situ measurements of ϵ_m, we conducted the following test to obtain an estimate of ϵ_m. We first filled about 60 ml of water into a 100 ml measuring tube (1 inch in diameter) with a 1 ml measuring accuracy, and then slowly poured a small amount (a mass M_s of about 100 g) of oven-dried sands into the tube. The sand layer, formed in the measuring tube with a flat and horizontal surface, allowed us to read the bulk volume of sands V_s. This sand layer should have the loosest compaction, and its porosity should be close to ϵ_m. Thus, ϵ_m is obtained from $\epsilon_m = 1 - \rho_B/\rho_s$, where ρ_s is the sand's density and $\rho_B = M_s/V_s$ is the measured bulk density. For each type of sand the measurement was repeated three times, and yielded very consistent ($\pm O(10^{-3})$) results for ϵ_m. The ϵ_m-values obtained (shown in Table 1) are between $0.4 \sim 0.5$ with the coarse sands having the highest value, 0.482, which is realistic for well-sorted sands [see e.g. *Fetter*, 2000].

It should be pointed out that the change of porosity of a bed with $\epsilon \approx \epsilon_m$ due to bed compaction can be quite significant. To confirm this, a standard shake-table test was performed as follows. About 1.8 kg oven-dried sand were slowly poured into a cylindrical container and a 2-kg dead weight was applied on top of the sample. The container was then shaken on a shaking table to gradually compact the sample until no significant change of the sample's bulk volume was observed. During each test the sample quickly compacted within the first few minutes and the reduction of porosity was about 0.1.

3.2. Test conditions

A summary of the tests conducted is provided in Table 2. In this study we only consider sinusoidal oscillatory flows characterized by a free-stream velocity

$$u_\infty(t) = U_{bm} \cos \omega t \qquad (3)$$

where U_{bm} is the velocity amplitude and $\omega = 2\pi/T$ is the angular frequency with T being the period. According to *Madsen* [1993], sheet-flow conditions under periodic sinusoidal waves are achieved if the following Shields parameter criterion is satisfied

$$\psi_{wmd} = \frac{\tau_{wmd}}{\rho(s-1)gd_{50}} = \frac{f_{wd}U_{bm}^2}{2(s-1)gd_{50}} > 0.7 \quad (4)$$

where τ_{wmd} is the maximum bottom shear stress based on a Nikuradse equivalent sand-grain roughness $k_N = d_{50}$. The corresponding wave friction factor f_{wd} is obtained from the wave friction factor formula given by *Humbyrd* [2012] (with $k_N = d_{50}$)

$$f_w = \exp[5.70(\frac{A_{bm}}{k_N})^{-0.101} - 7.46], \quad 10 < \frac{A_{bm}}{k_N} < 10^5 \quad (5)$$

Based on this criterion, we are able to choose three flow conditions for the medium-sand bottom, two flow conditions for the fine-sand bottom but only one flow condition, which is close to the design limit of the WCS, for the coarse-sand bottom. The values of U_{bm} in Table 2 are target values predicted from the specified piston motion, and it has been demonstrated by *Yuan and Madsen* [2014] that these target values can be taken as the actual free-stream velocities with an accuracy of the order 1 cm/s.

For each flow-sediment condition, tests are performed for five bottom slopes from 0.10° to 2.60°. Before most tests, the movable bed is flattened with the reading of slope meter being 0.00°, and then tilted to the specified slope. Since the WCS and the CSB are tilted in unison, the slope can be produced with the accuracy of slope meters placed on both of them, i.e. 0.01°, and the flat bottom will appear to be horizontal on the camera images. Similar to some previous sheet-flow experiments in oscillatory water tunnels, e.g. *van der A et al.* [2010], our tests last for 20-50 periods. This test duration is long enough to neglect initial conditions, i.e. the suspension of sediments reaches an equilibrium state within 1-3 periods based on our visual observations, and is also short enough to avoid end effects occupying the entire facility. Some tests are repeated to evaluate the repeatability (see Table 2), and to estimate our experimental accuracy by evaluating the discrepancy. The last two columns in Table 2 refer to experimental results of net transport rate that will be discussed in section 4.3.

3.3. Determination of net sediment transport rates

There are mainly two different methods used in previous studies to obtain sediment transport rates in an OWT: trap-collection [e.g. *King*, 1991] and volume-conservation methods [e.g. *van der A et al.*, 2010]. For the trap-collection method, the difference between the volumes of sediments collected in traps located at the two ends of the test section is used to calculate the net transport rate. Although this method is convenient to apply, the measurements are strongly influenced by end effects, e.g. scour pits at the ends of the sand bed change local flow and sediment transport, which can penetrate into the test section by a distance of $O(A_{bm})$, where A_{bm} is the excursion amplitude of the free-stream oscillatory flow. The volume-conservation method, which avoids these "end problems", is based on the principle of volume conservation as follows. The sediment transport rate q_s can be related to the change of bottom elevation z_b through

$$\frac{\partial q_s}{\partial x} = -(1-\epsilon)\frac{\partial z_b}{\partial t} \tag{6}$$

where ϵ is bed porosity, t is time and x is the longitudinal coordinate which is taken positive in the upslope direction in this study. Integrating equation (6) over x from the downslope end $x = x_0$ gives an estimate of $q_s(x,t)$ along the test section

$$q_s(x,t) = q_{s,0} - \int_{x_0}^{x} (1-\epsilon)\frac{\partial z_b}{\partial t} dx \tag{7}$$

where $q_{s,0}$ is an integral constant corresponding to the sediment transport rate through $x = x_0$ at time t. Except for the initial stage of an experiment, the period-averaged net transport rate should be in equilibrium, and therefore can be estimated by averaging equation (7) over the test duration ΔT, which gives

$$q_{sd}(x) = -\frac{1-\epsilon}{\Delta T}\int_{x_0}^{x}\Delta z dx - \frac{V_0}{\Delta T b} \tag{8}$$

where $q_{sd}(x)$ is net transport rate (subscript d indicates starting the integral from the downslope end), V_0 is the volume of sand collected from $x < x_0$, b is the width of the section, ΔT is the test duration and Δz is the change of bottom elevation during an experiment. Thus, $q_{sd}(x)$ can be obtained from the measurement of Δz. In the region sufficiently far from the two ends, the obtained $q_{sd}(x)$ should be fairly uniform due to the longitudinal uniformity of flow condition in the WCS, and this equilibrium net sediment transport rate is taken as the final measurement. Starting the integral from the upslope end of the test section $x = x_L$ gives another estimate

$$q_{su}(x) = \frac{1-\epsilon}{\Delta T}\int_{x}^{x_L}\Delta z dx + \frac{V_L}{\Delta T b} \tag{9}$$

where V_L is the volume of sand collected from $x > x_L$ after one experiment. Equations (8) and (9) are expected to give the same results, i.e.

$$q_{sd}(x) - q_{su}(x) = \frac{1}{\Delta T b}[V_{LBP} - (V_0 + V_L)] = 0 \tag{10}$$

where

$$V_{LBP} = -(1-\epsilon)b\int_{x_0}^{x_L}\Delta z dx \tag{11}$$

represents the measured sediment volume lost from the test section, $x_0 \leq x \leq x_L$. To satisfy conservation of total sediment volume within the test facility V_{LBP} must equal the sediment volume collected outside the test section, i.e. $V_0 + V_L$, rendering the right hand side of equation (10) zero and resulting in $q_{sd}(x) = q_{su}(x)$. This, however, is not so when we evaluate equation (10) using our experimentally obtained values of Δz, V_0, and V_L. In all our experiments the right hand side of equation (10) turns out to be > 0, i.e. suggesting that more sediment is lost from within than recovered outside the test section.

We hypothesize that this physically unrealistic result is caused by a uniform compaction of the 20-cm-deep layer of loosely packed sand placed in the test section by an amount, δz, given by

$$\delta z = \frac{V_{LBP} - (V_0 + V_L)}{(1-\varepsilon)Lb} \tag{12}$$

where $L = x_L - x_0$ is the length of LBP coverage. Replacing our measured Δz by its compaction-corrected value,

$$\Delta z_C(x) = \Delta z + \delta z \tag{13}$$

we obtain the corrected net transport rate from

$$q_s(x) = -\frac{(1-\epsilon)}{\Delta T}\int_{x_0}^{x} \Delta z_C(x)dx - \frac{V_0}{\Delta T b} \tag{14}$$

where the subscript "*d*" has been omitted, since starting from upslope or downslope end would give identical transport rates now that total sediment volume in the facility is conserved. Evidence in support of our compaction-hypothesis will be presented in section 4.2 when this methodology is applied in the analysis of our data, along with a discussion of potential causes for the compaction as well as alternative methodologies for the determination of net sediment transport rates when conservation of total sediment volume is violated.

4. Experimental results

4.1. Typical observations of bottom profile change

Since net sediment transport rate is obtained from measured bottom elevation change Δz, we first present typical observations of Δz. It should be noted that Δz can also be taken as the final bottom profile for tests started with a flat bed. Figure 2 shows the measured Δz for three F1 fine-sand tests ($U_{bm} = 0.90$ m/s, $T = 4.17$ s, $A_{bm} = U_{bm}/\omega = 60$ cm, $d_{50} = 0.13$ mm) over three bottom slopes ($\beta = 0.10°, 1.10°$ and $2.60°$). The net sediment transport rate for most tests is in the downslope direction (towards the left in Figure 2), so a relatively big scour pit is developed near the upslope end (800 cm$< x <$900 cm), while near the downslope end (0 cm$< x <$100 cm), a relatively smaller scour pit (e.g. F1_S11) or even a deposition hump (e.g. F1_S26) is developed, depending on the magnitude of net transport rate. These bottom features are actually very mild, as their vertical scale (a few cm) is much smaller than their horizontal scale ($\sim O(A_{bm}) \sim O(100$ cm)). Around the middle of the test section (200 cm$< x <$700 cm), the movable bed remains essentially flat with a Δz fluctuating around zero by ± O(1 mm), which indicates that the net transport rate in this region is fairly uniform.

For the three groups of tests with the lowest three Shields parameter ψ_{wmd} (0.89∼1.20, see Table 2), i.e. two groups of medium-sand tests (M1 and M2) and the coarse-sand test (C1), bedforms of vanishingly small steepness are observed to develop, even though the experiments are supposed to be in the sheet-flow regime. This is not surprising, as the $\psi_{wmd} = 0.7$ threshold in equation (4) should not be taken as a clear cut lower limit for sheet-flow regime with a perfectly flat bed. Figure 3a compares the final bottom profiles after running a M2 test ($U_{bm} = 1.21$ m/s, $T = 6.25$ s, $d_{50} = 0.24$ mm) over a 0.60° slope for 25 and 50 periods. As we can see, reasonably periodic bedforms are developed by the oscillatory flow. The bedform height is about 5 mm after the first 25 periods, but grows to about 10 mm after 50 periods, while the bedform length seems to be invariant ($\sim$150 cm). The reason for these bedforms is still unclear, but the height-to-length ratio is less than 1/100, and no flow separation or vortex cloud of suspended sands is observed, so we can still consider the experiment to be in the sheet-flow regime.

4.2. Bed compaction

The 20 cm-deep movable bed in the test section is prepared by slowly depositing sands, and the surface 1-2cm layer is disturbed after flattening the bed before most tests. Therefore, a slight bed compaction will occur either due to the sheet-flow, which will shake up the surface 1-2cm layer of sands, or a pressure-gradient ($\partial p/\partial x$)-induced flow within the stationary porous bed. The oscillatory flow can be always assumed uniform along the test section, because the change of bottom profile is immaterial compared to the channel height (50 cm), as demonstrated in Figures 2 and 3a. Consequently, it can be hypothesized that the flow-induced bed compaction will be fairly uniform along the entire movable bed and can be quantified as a homogeneous settling δz given by equation (12). Based on all tests, δz is always positive with a mean value of 0.2 mm and a standard deviation of 0.16 mm, indicating that bed compaction indeed occurs. If a conservative assumption is made that only the surface 1 cm layer of the movable bed is compacted, i.e. attributing the compaction entirely to sheet-flow disturbance, a 0.2 mm compaction corresponds to only a decrease in porosity of 0.01, which is much smaller than the maximum possible decrease of porosity, i.e. about 0.1, suggested by the shake-table tests. Such a slight compaction should not influence the sediment transport processes, and therefore is not a concern for the validity of our experiments. To further confirm that the obtained δz is due to compaction, three pairs of M2 tests (U_{bm}=1.21 m/s, T =6.25 s, d_{50}=0.24 mm) over three bottom slopes are performed. In each pair, the second test used the movable bed left by the first test, i.e. the movable bed after the first test was not reworked before the second test. Since the movable bed had been pre-compacted by the first test, less compaction or smaller δz is expected for the second test, which is confirmed by the δz values shown in Table 3. It should be pointed out that the discrepancy between the net sediment transport rates for each pair of tests (last two columns of Table 3) is within our experimental inaccuracy $\Delta q \sim O(10^{-6} m^2/s)$ (discussed in section 4.3). Therefore, it is not necessary to conduct experiments in pairs just to reduce bed compaction.

Bed compaction will lead to a "violation" of volume conservation for sand, which is a possible reason for the mismatch between the two net transport rates integrated from the two ends, i.e. equation (10) is not satisfied. Therefore, we have proposed a bed-compaction correction in section 3.3, i.e. equations (12)-(14), which essentially attributes the mismatch totally to an overestimate of V_{LBP} due to a uniform compaction in the test section. Alternatively, we can also attribute the mismatch entirely to the error in the volume of sand collected outside the integral boundaries, i.e. V_0 and V_L. We choose a correction, $\Delta V = V_{LBP} - (V_0 + V_L)$, for V_0 and V_L, and take $V_{0,C} = V_0 + \Delta V/2$ and $V_{L,C} = V_L + \Delta V/2$, since the two ends are virtually identical. This will lead to another correction for net transport rate, which is equivalent to taking a simple average between q_{su} and q_{sd} given by equations (8) and (9)

$$q_{sA}(x) = \frac{q_{su}(x) + q_{sd}(x)}{2} \tag{15}$$

In many previous studies [e.g. *Hassan and Ribberink*, 2005; *van der A et al.*, 2010], this simple-average correction is adopted, and the transport rate at the middle point ($x = x_0 + L/2$) is taken as the final equilibrium net transport rate. To show that the two corrections are not equivalent, we simply subtract equation (14) from equation (15). With some simple algebra we obtain

$$q_{sA}(x) - q_s(x) = \frac{(1-\epsilon)}{\Delta T}\delta z(x - x_0 - \frac{L}{2}) \quad (16)$$

Thus, the two corrections are only identical at the middle point ($x = x_0 + L/2$) of the test section.

We further compare these two corrections based on a typical test M2_S11 shown in Figure 4. For this test our bed-compaction correction (the solid line) gives a fairly uniform transport rate around the middle point, so an expected central region with an equilibrium net transport rate is indeed established, which also supports the assumption of a uniform bed compaction over the entire test section. The simple-average correction (the dash-dot line), however, gives a net transport rate increasing towards the upslope (right) end around the middle point, so one could argue that this experiment fails to reach the expected equilibrium state and therefore is invalid. Therefore, our bed-compaction correction supersedes the simple-average correction in that it can yield results demonstrating the validity of a test. Another argument against the simple-average correction is as follows. In our experiments, the mismatch in volume, $\Delta V = V_{LBP} - (V_0 + V_L)$, usually corresponds to about 1 kg of sand, while our accuracy in collecting sands from the two ends is estimated to be about 0.1 kg. Thus, ΔV is very unlikely due to the experimental error in collecting V_0 and V_L, which invalidates the assumption of the simple-average correction.

It should be pointed out that the simple-average correction is quantitatively equivalent to the proposed bed-compaction correction, if the computed value of q_s at the middle point $x = x_0 + L/2$ is taken as the equilibrium transport rate. Thus, we do not question the validity of previous studies adopting the simple-average correction. However, this may not be true for tests with very low q_s or significant spatial variation of q_s due to the presence of low-steepness bedforms (see section 4.1).

4.3. Net transport rate

The obtained net sediment transport rate is averaged over the equilibrium region to give the final measurement $q_{s,net}$

$$q_{s,net} = \frac{\int_{x_1}^{x_2} q_s(x)dx}{x_2 - x_1} \tag{17}$$

where x_1 and x_2 are the limits for averaging. Since water particles within $2A_{bm}$ from the ends can reach the ends, we simply take $2A_{bm}$ as an initial rough estimate of the influential range of end effects, and set $x_1 = x_0 + 2A_{bm}$ and $x_2 = x_L - 2A_{bm}$, where $x_0 = 95$ mm and $x_L = 8905$ mm are the coordinates of the downslope and upslope ends of the movable bed, respectively. As shown in Figure 3b, for tests with the presence of low-steepness bedforms, there may be a quite significant spatial variation of q_s, because the local bottom slope can be comparable to mean slope ($1/100 \sim 0.6°$). Therefore, the two limits for averaging are further adjusted to include an integer number of bedforms. As seen from Table 2, for instance test M2_S06, the net transport rates averaged over integer numbers of bedforms are almost the same after 25 and 50 periods, which confirms that the bedforms have little effect on the net transport rate in the equilibrium region, as long as the spatial variation is taken care of by averaging.

The second to last column of Table 2 presents the experimental results for $q_{s,net}$, whereas the last column presents $\Delta q_{net} = |q_{net,a} - q_{net,b}|/2$, the difference between repeated experiments ($q_{net,a}$ and $q_{net,b}$), except for test M2_S26, for which Δq_{net} is the standard deviation of the four repeats. The obtained $\Delta q_{s,net}$ is of the order $1 \cdot 10^{-6}$m^2/s, which is generally much smaller than the magnitude of the corresponding $q_{s,net}$, demonstrating that the experiments are highly repeatable. We therefore can use the averaged $q_{s,net}$ from repeats as the final measurement for that particular test condition and take $1 \cdot 10^{-6}$m^2/s as the estimate of the accuracy of our determination of $q_{s,net}$. For a given flow-sediment condition, the test with a 0.10° slope has a net transport rate of the same order as the experimental accuracy ($1 \cdot 10^{-6}$m^2/s), which agrees with the expectation that a zero net transport rate should be obtained for horizontal bottoms. For the rest of the tests, $q_{s,net}$ is always in the downslope direction (negative values) and increases with bottom slope.

The magnitude of $q_{s,net}$ for tests on our maximum slope (2.60° or 1 on 22) is generally between $(2 \sim 5) \cdot 10^{-5}$m^2/s, which is comparable to the $q_{s,net}$ due to flow skewness obtained in some previous OWT sheet-flow studies. For example, the flow and sediment conditions in our M3 tests are comparable to those in the Series-B-16 test by *Ribberink and Al-Salem* [1994] (d_{50}=0.21 mm, 6.5 s-period asymmetric oscillatory flows corresponding to Stokes 2nd-order waves with the maximum and minimum velocities being 1.72 m/s and -0.86 m/s, respectively). The measured transport rate in this test, $q_{s,net} = 70 \cdot 10^{-6}$m^2/s, is comparable to that in M3_S26, $q_{s,net} = -54 \cdot 10^{-6}$m^2/s. It should be noted that the flow skewness of the quoted test even exceeds the limit of Stokes 2nd-order waves theory, i.e. the maximum flow velocity should be less than 5/3 times the minimum flow velocity, but the actual bottom slope in surf zones can be larger than our maximum value. Therefore, our results suggest that the slope effect may be as important as wave nonlinearity and therefore should be included in predictions of cross-shore $q_{s,net}$. A more quantitative comparison of these two effects requires extensive future research work, e.g. additional experiments of skewed oscillatory flows over sloping bottoms which are not within the scope of the present study.

For a given flow-sediment condition, the net sediment transport rate $q_{s,net}$ is only a function of bottom slope β, i.e. $q_{s,net} = f(\beta)$, which can be approximated for mild slopes with a Taylor-series expansion

$$q_{s,net} = f(\beta = 0) + \left.\frac{\partial f}{\partial \beta}\right|_{\beta=0} \beta + O(\beta^2) \approx A' \cdot \beta \quad (18)$$

in which the constant A' depends on the flow and sediment conditions and has a unit of, for example, m^2/s with β in radians. This suggests that the magnitude of $q_{s,net}$ should increase linearly with β. Since most of the measured net transport rates are in the downslope direction (negative $q_{s,net}$), we introduce

$$q_{net} = -q_{s,net} = A \cdot \beta \quad (19)$$

where $A = -A'$ is always positive. The net sediment transport rate is plotted against β for each flow-sediment condition in Figure 5. The data points suggest that q_{net} indeed increases linearly with β, so equation (19) is therefore fitted to the measurements. Table 4 shows the results of linear-function fittings. The coefficient of determination R^2 is over 0.93, and the relative 95%-confidence interval, ΔA, for A is less than 22%, indicating a good fitting quality. More discussion of this linear relationship will be provided in section 5.

4.4. Lateral inhomogeneity

Our experimental method assumes that the net sediment transport rate is laterally uniform, which can be invalidated by many factors, e.g. imperfect initial bed preparation, sidewall effects or three-dimensionality of end effects, so it is necessary to assess the influence of lateral inhomogeneity on the experimental determination of net transport rate. Since the LBP has two laser lines giving two measurements of bottom elevation change, Δz_1 and Δz_2, along two lateral positions of the WCS, we can separately use them to obtain two estimates of net transport rate, $q_{net,1}$ and $q_{net,2}$, following the same data analysis method introduced before. The obtained net transport rate based on single laser lines still exhibit good linear dependency on bottom slope for a given flow-sediment condition, so following the analysis in section 4.3 we fit the linear function, i.e. $q_{net,i} = A_i \cdot \beta$ $(i = 1, 2)$, between net transport rate $q_{net,i}$ and bottom slope β, and investigate the effect of lateral inhomogeneity based on the fitted slopes A_i ($\pm 95\%$ confidence limits in %). As shown in Table 5, the discrepancies among the obtained A_i, expressed by the ratio $|A_1 - A_2|/(2A)$, are about $10 \sim 20\%$ for tests with coarse and medium sands, while for fine-sand tests the discrepancies are quite immaterial ($O(2\%)$). Since low-steepness bedforms are only observed for tests with coarse and medium sands, they are likely the main reason for lateral inhomogeneity. Nevertheless, an uncertainty of $10 \sim 20\%$ is generally considered acceptable in the study of sediment transport, indicating that we can neglect the lateral inhomogeneity.

5. A conceptual model

In this section we present a conceptual model for predicting bottom-slope-induced net sheet-flow sediment transport rate. Following the single-phase approach, we separately develop models for both net bedload and suspended-load transport rates, which allow us to understand the mechanisms through which the bottom slope produces a net transport rate. The model does not account for some details within the thin sheet-flow layer, e.g. the inter-granular processes, so the predictions of flow velocity and sediment concentration are conceptual in the close vicinity of the sand bed. Nevertheless, the model parameters are determined carefully to ensure a valid prediction of the net sediment transport rate.

5.1. Net bedload transport rate

The net bedload transport rate is predicted by period-averaging the prediction of instantaneous bedload transport rate

$$\bar{q}_{sB} = \frac{1}{T}\int_0^T q_{sB}(t)dt \tag{20}$$

The sands in our study have diameters from 0.13 to 0.51 mm, so their response time to changing flow is much shorter than a flow period. Thus, the instantaneous bedload transport rate can be calculated with the instantaneous flow condition in a quasi-steady manner with a bedload transport model, which accounts for the effect of bottom slope.

The model proposed by *Madsen* [1993], which extended his conceptual bedload transport model [*Madsen*, 1991] to account for a bottom slope effect, is adopted in this study. *Gonzalez-Rodriguez and Madsen* [2007] successfully applied this model to predict the experimental bedload transport rates obtained by *King* [1991] for his bedload-dominated cases, which supports our adoption of this model. This model considers an exposed spherical sediment grain of diameter d and specific density s resting on a plane bed inclined at an angle β to horizontal, where β is taken positive if sloping upward in the direction of transport, as shown in Figure 6. A force balance in the bottom-parallel direction can be written as

$$F_{fD} - F_{gx} = F_R = F_{g\perp} \cdot \begin{cases} \tan\phi_s, & \text{incipient motion} \\ \tan\phi_m, & \text{bedload transport} \end{cases} \qquad (21)$$

where F_{fD} is the fluid drag force, F_{gx} is the bottom-parallel component of the submerged weight, and F_R is the frictional resistance, which is given by the product of $F_{g\perp}$ (the bottom-normal component of the submerged weight) and an angle of friction, i.e. ϕ_s for static friction and ϕ_m for moving friction. *Madsen* [1991] suggested that $\phi_s = 47°$ and $\phi_m = 28°$, in agreement with the experimental value obtained by *King* [1991].

Comparing equation (21) for incipient motions on horizontal and sloping bottoms, it can be easily shown that the critical Shields parameter for sands on a sloping bottom, $\psi_{cr,\beta}$, can be expressed as

$$\psi_{cr,\beta} = \frac{u_{*cr}^2 F_s(\beta)}{(s-1)gd} = \psi_{cr} F_s(\beta) \qquad (22)$$

where ψ_{cr}, the critical Shields parameter for a horizontal bottom, is determined from the modified Shields diagram proposed by *Madsen and Grant* [1976], u_{*cr} is the critical shear velocity corresponding to ψ_{cr}, and $F_s(\beta)$ is a slope correction factor given by

$$F_s(\beta) = \cos\beta \left(1 + \frac{\tan\beta}{\tan\phi_s}\right) \qquad (23)$$

The bedload sediment transport rate is obtained with the knowledge of average sediment grain velocity, u_s, and the number of bedload sediment grains per unit surface area, N_B. Starting from the bottom-parallel force balance, i.e. equation (21), but otherwise following *Madsen* [1991], we obtain

$$u_s = 8\left(u_* - u_{*cr}\sqrt{\frac{1}{2}F_m(\beta)}\right) \qquad (24)$$

where u_* is the shear velocity related to the driving bottom shear stress and $F_m(\beta)$ is a correction factor for bottom slope

$$F_m(\beta) = \cos\beta \left(1 + \frac{\tan\beta}{\tan\phi_m}\right) \tag{25}$$

Assuming that the excess bottom shear stress $\tau_b - \tau_{cr,\beta}$ is balanced by the drag force on moving sediment grains, the number of sediment grains in motion per unit bottom area is

$$N_B = \frac{u_*^2 - u_{*cr}^2 F_s(\beta)}{\tan\phi_m \left(\frac{\pi}{6}d^3\right)(s-1)gF_m(\beta)} \tag{26}$$

and the bedload transport rate is obtained from

$$\begin{aligned} q_{sB} &= N_B \left(\frac{\pi}{6}d^3\right) u_s \\ &= \frac{8}{\tan\phi_m (s-1)gF_m(\beta)} \left(u_*^2 - u_{*cr}^2 F_s(\beta)\right) \left(u_* - u_{*cr}\sqrt{\frac{1}{2}F_m(\beta)}\right) \end{aligned} \tag{27}$$

We hereafter denote this as the M93 formula. For very mild bottom slope ($\tan\beta \approx \beta \ll 1$), the primary effect of bottom slope is represented by the $F_m(\beta)$ term in the denominator, i.e.

$$q_{sB,\beta} \approx q_{sB,0}(1 - \frac{\beta}{\tan\phi_m}) + O(\tan\beta^2) \tag{28}$$

where $q_{sB,0}$ is the corresponding bedload transport rate over a horizontal bottom. Thus, the effect of bottom slope on the instantaneous bedload transport rate is simply a factor of $\beta/\tan\phi_m$.

Following the quasi-steady assumption, the instantaneous bedload transport rate can be predicted with the instantaneous bottom shear stress as

$$\begin{aligned} q_{sB}(t) = &\frac{8}{\tan\phi_m (s-1)gF_m(\beta(t))} \cdot \\ &\max\left[u_{*d}(t)^2 - u_{*cr}^2 F_s(\beta(t)), 0\right] \left(u_{*d}(t) - u_{*cr}\sqrt{\frac{F_m(\beta(t))}{2}}\right) \frac{\tau_{bd}(t)}{|\tau_{bd}(t)|} \end{aligned} \tag{29}$$

where

$$\beta(t) = \begin{cases} \beta, & \tau_{bd}(t) > 0 \quad \text{(upslope)} \\ -\beta, & \tau_{bd}(t) \leq 0 \quad \text{(downslope)} \end{cases} \tag{30}$$

and the subscript "d" has been added to shear stress related terms to reflect the derivation of the M93 formula, and hence equation (29), being based on an assumed bottom roughness equal to the diameter of the sediment grains.

Yuan and Madsen [2014] experimentally and theoretically showed that for sinusoidal oscillatory boundary layers the time-varying bottom shear stress can be accurately approximated by a first and a third harmonic

$$\tau_{bd}(t) = \alpha \tau_{wmd} \cos(\omega t + \varphi_\tau) + (1 - \alpha) \tau_{wmd} \cos(3\omega t + 3\varphi_\tau) \tag{31}$$

where τ_{wmd} is the maximum bottom shear stress and φ_τ is the phase lead of τ_{wmd} relative to the maximum free-stream velocity. Measurements confirm the theoretical prediction that the ratio of the third-harmonic amplitude to the first-harmonic amplitude is about 15%, so α is set to 0.87. Model validation by *Yuan and Madsen* [2014] suggests that both τ_{wmd} and φ_τ can be accurately predicted by the wave boundary layer model developed by *Humbyrd* [2012] from knowledge of the free-stream velocity and bottom roughness

$$\tau_{wmd} = \frac{1}{2} \rho f_w {U_{bm}}^2 \tag{32}$$

with the friction factor f_w given by equation (5), and

$$\varphi_\tau [rad] = 0.649 \left(\frac{A_{bm}}{k_N} \right)^{-0.160} + 0.118, \quad 10 < \frac{A_{bm}}{k_N} < 10^5 \tag{33}$$

Thus, equations (31) to (33) enable us to predict the instantaneous bottom shear stress. To be consistent with the fact that the bedload transport model, i.e. equations (27) and (29), is derived based on $k_N = d$, τ_{wmd} and φ_τ are predicted using $k_N = d_{50}$.

Figure 7 shows the predicted $\tau_{bd}(t)$ and instantaneous bedload transport rate $q_{sB}(t)$ for test M3_S26 (U_{bm}=1.6 m/s, T=6.25 s, d_{50}=2.4 mm, and β=2.6°). To facilitate comparison between temporal variations, q_{sB} and τ_{bd} are normalized by their upslope (positive) maxima. Since q_{sB} is approximately scaled by $\tau_{bd}^{3/2}$, the predicted q_{sB} has sharper crests than τ_{bd}. The downslope minimum of q_{sB} is about 20% larger than the upslope maximum, which agrees with the effect of bottom slope suggested by equation (28), i.e. $2\beta/\tan\phi_m \approx 17\%$.

5.2. Net suspended-load transport rate

The net suspended-load transport rate is given by

$$\bar{q}_{sS} = \int_{z_r}^{\infty} \overline{uc} dz \tag{34}$$

where the over-bar indicates period-averaging, z_r is a reference level, u is velocity and c is volumetric concentration. For sinusoidal oscillatory boundary layers, we can express u as a Fourier series with only odd-order harmonics due to the perfect asymmetry between successive half-periods

$$u = \sum_{n=0}^{\infty} \mathrm{Re}(U_{2n+1} e^{i\varphi_{u,2n+1}} e^{i(2n+1)\omega t}) \tag{35}$$

where U_{2n+1} and $\varphi_{u,2n+1}$ are the amplitude and phase of the $(2n+1)$th-harmonic velocity. Similarly, the concentration can also be expressed as a Fourier series

$$c = \bar{c} + \sum_{n=1}^{\infty} \mathrm{Re}(c_n e^{i\varphi_{c,n}} e^{in\omega t}) \tag{36}$$

where $\bar{c}$ is the mean concentration, and c_n and $\varphi_{c,n}$ are the amplitude and phase of n-th harmonic concentration, respectively. The net sediment flux at a given vertical level can then be written as

$$\overline{uc} = \frac{1}{2} \sum_{n=0}^{\infty} U_{2n+1} c_{2n+1} \cos\left(\varphi_{u,2n+1} - \varphi_{c,2n+1}\right) \tag{37}$$

If the bottom is horizontal, the temporal variation of concentration should have two identical half-periods, so all odd harmonics of concentration vanish, leading to a zero net suspended-load transport rate. However, for a sloped bottom equation (26) suggests that the number of bedload sand grains, N_B, deviates from the corresponding zero-slope value, and can be approximated by

$$N_B \approx N_{B,0}(1 - \frac{\beta}{\tan\phi_m}) \tag{38}$$

where $N_{B,0}$ is the number of bedload sediment grains for the same flow on a horizontal bottom, i.e. with $\beta = 0$ in equation (26). Thus, the variation of N_B with β is a factor of $1-\beta/\tan\phi_m$ (minus sign indicates less moving sand grains for upslope flow). The reference sediment concentration, which is usually defined at a few sediment diameters above the bottom, should be proportional to the number of moving sand grains considered as bedload transport, i.e. $c_r \propto N_B$. It is also reasonable to assume that reference concentration responds to the change of bedload transport rate in a quasi-steady manner, so the two half-periods of reference concentration are slightly asymmetric due to bottom slope, as shown in Figure 8. The difference between the peaks of $c_r(t)$ can be represented by a first-harmonic reference concentration

$$c_{r1}(t) = c_{rm,0}\frac{\tan\beta}{\tan\phi_m}\cos(\omega t + \varphi_{rc1}) \tag{39}$$

where $c_{rm,0}$ is the maximum reference concentration for the same flow-sediment condition on a horizontal bottom. Since the slope is defined positive in the upslope direction, the phase φ_{rc1} should be related with the phase lead of the effective bottom shear stress φ_τ (predicted using equation (33) with $k_N = d_{50}$) through

$$\varphi_{rc1} = \varphi_\tau + \pi \tag{40}$$

This first-harmonic reference concentration is diffused upward into the water column, so a first-harmonic concentration is developed. Higher-order odd harmonics of velocity are negligible compared to the first harmonic [*Yuan and Madsen*, 2014], so the mean sediment flux can be well approximated by the first-harmonic terms, i.e.

$$\overline{uc} \approx \frac{1}{2} U_1 c_1 \cos\left(\varphi_{u1} - \varphi_{c1}\right) \tag{41}$$

The net suspended-load transport rate is therefore

$$\bar{q}_{sS} = \int_{z_r}^{\infty} \frac{1}{2} U_1 c_1 \cos\left(\varphi_{u1} - \varphi_{c1}\right) dz \tag{42}$$

The remaining task is to predict the first-harmonic velocity and concentration, and then numerically evaluate the integral defined by equation (42).

5.2.1. First-harmonic velocity

The governing momentum equation for oscillatory turbulent boundary layers in OWTs is

$$\frac{\partial u}{\partial t} = \frac{\partial u_\infty}{\partial t} + \frac{\partial}{\partial z}\left(\frac{\tau_{zx}}{\rho}\right) \tag{43}$$

where t is time, z is the vertical coordinate, ρ is water density, τ_{zx} is the Reynolds shear stress and u_∞ is the free-stream velocity. τ_{zx} can be related to the vertical velocity gradient through a turbulent eddy viscosity ν_T

$$\frac{\tau_{zx}}{\rho} = \nu_T \frac{\partial u}{\partial z} \tag{44}$$

Following *Grant and Madsen* [1979], we adopt their simple time-invariant

$$\nu_T = \kappa u_{*f} z \tag{45}$$

where $\kappa = 0.4$ is von Karman's constant and u_{*f} is chosen as the shear velocity based on maximum bottom shear stress. Equation (43) can now be written as

$$\frac{\partial u}{\partial t} = \frac{\partial u_\infty}{\partial t} + \frac{\partial}{\partial z}\left(\nu_T \frac{\partial u}{\partial z}\right) \tag{46}$$

Solving equation (46) with the following boundary conditions

$$\begin{cases} u = 0, \quad z = z_0 = k_N/30 \\ u \to u_\infty = U_{bm}\cos(\omega t), \quad z \to \infty \end{cases} \tag{47}$$

we get the complex-amplitude of the first-harmonic velocity

$$U^{(1)}(z) = U_1 e^{i\varphi_{u1}} = U_{bm}\left[1 - \frac{\mathrm{ker}(2\sqrt{\frac{z}{l}}) + i\mathrm{kei}\,(2\sqrt{\frac{z}{l}})}{\mathrm{ker}(2\sqrt{\frac{z_0}{l}}) + i\mathrm{kei}(2\sqrt{\frac{z_0}{l}})}\right] \tag{48}$$

where ker and kei are Kelvin functions of order zero, see *Abramowitz and Stegun* [1965], and l is a boundary-layer length scale defined as

$$l = \frac{\kappa u_{*f}}{\omega} \tag{49}$$

In the very near-bottom region, the amplitude of first-harmonic velocity converges to a logarithmic profile scaled by u_{*f}, which is confirmed by many measurements [e.g. *Yuan and Madsen*, 2014]. The closure for u_{*f} and the choice of k_N will be discussed later in conjunction with other model parameters (section 5.3).

5.2.2. First-harmonic concentration

Since the flow in OWTs is homogeneous in the stream-wise direction, the governing equation for sediment concentration is

$$\frac{\partial c}{\partial t} = w_f \frac{\partial c}{\partial z} + \frac{\partial}{\partial z}(D_T \frac{\partial c}{\partial z}) \tag{50}$$

where w_f is the sediment fall velocity and D_T is the turbulent diffusivity. Assuming sediments to be passive, a close analogy can be drawn between the turbulent diffusion of momentum and sediment. Thus for internal consistency with equation (45) we take

$$D_T = \kappa u_{*D} z \tag{51}$$

where u_{*D} is a characteristic shear velocity. Using complex variables, we can write the first-harmonic concentration as

$$c_1(z,t) = \mathrm{Re}\left(c^{(1)}(z)e^{\mathrm{i}\omega t}\right) \tag{52}$$

where $c^{(1)}$ is the complex amplitude, and the governing equation for $c^{(1)}$ is

$$i\omega c^{(1)} = w_f \frac{\partial c^{(1)}}{\partial z} + \frac{\partial}{\partial z}(D_T \frac{\partial c^{(1)}}{\partial z}) \tag{53}$$

which can be normalized into

$$\mathrm{i}\hat{c}^{(1)} = a\frac{\partial \hat{c}^{(1)}}{\partial \xi} + \frac{\partial}{\partial \xi}\left(\xi \frac{\partial \hat{c}^{(1)}}{\partial \xi}\right) \tag{54}$$

with:

$$\hat{c}^{(1)} = \frac{c^{(1)}}{c_r{}^{(1)}} \tag{55}$$

$$a = \frac{w_f}{\kappa u_{*D}} \tag{56}$$

$$\xi = z/\left(\frac{\kappa u_{*D}}{\omega}\right) \tag{57}$$

where

$$c_r^{(1)} = c_{rm,0}\frac{\tan\beta}{\tan\phi_m}e^{i\varphi_{rc1}} \tag{58}$$

is the complex amplitude of the first-harmonic reference concentration specified at a reference level $z = z_r$. The boundary conditions for the normalized governing equation are

$$\begin{cases} \hat{c}^{(1)} = 1 & \xi = \xi_r = z_r/\left(\frac{\kappa u_{*D}}{\omega}\right) \\ \hat{c}^{(1)} \to 0 & \xi \to \infty \end{cases} \tag{59}$$

The analytical solution of this set of equations

$$\hat{c}^{(1)} = \frac{\xi^{-a/2}\left[\mathrm{ker}_a\left(2\sqrt{\xi}\right) + \mathrm{ikei}_a\left(2\sqrt{\xi}\right)\right]}{(\xi_r)^{-a/2}\left[\mathrm{ker}_a\left(2\sqrt{\xi_r}\right) + \mathrm{ikei}_a\left(2\sqrt{\xi_r}\right)\right]} \tag{60}$$

was given by *Wikramanayake* [1993] with $\mathrm{ker_a}$ and $\mathrm{kei_a}$ denoting Kelvin functions of order "a" [see *Abramowitz and Stegun*, 1965].

5.3. Determination of model parameters

Whereas all parameters needed to evaluate the bedload transport model presented in section 5.1, equation (29), have been defined, computation of the suspended-load transport model developed in section 5.2 requires the specification of several parameters: (i) the shear velocity and associated roughness needed to evaluate the advective velocity from equation (48), (ii) the sediment fall velocity, w_f, and (iii) the shear velocity, u_{*D}, scaling the turbulent eddy diffusivity are required to obtain the parameter, a, defined by equation (56); and (iv) the reference concentration, $c_{rm,0}$, and the level where it is specified, z_r, in order to predict the concentration distribution from equations (55) and (60).

To obtain these model parameters we make use of the results by *Zyserman and Fredsøe* [1994] (ZF94 hereafter), who analyzed an extensive set of laboratory data on total-load sediment transport rates obtained for steady uniform open channel flows to obtain an empirical formula for the reference concentration. Since ZF94 developed their formula from steady-flow data, we first review the salient features of their analysis, before we present our methodology to translate ZF94's steady flow results for our unsteady oscillatory flow conditions.

5.3.1. Summary of data analysis of ZF94

By splitting the measured total-load transport, q_{TM}, into bedload and suspended-load contributions, ZF94 obtained data on the latter from

$$q_{S,ZF} = q_{TM} - q_{B,ZF} \tag{61}$$

by predicting the bedload transport rate using the formula proposed by *Engelund and Fredsøe* [1976]

$$\frac{q_{B,ZF}}{\sqrt{(s-1)gdd}} = 5\left[1 + \left(\frac{\frac{\pi}{6}\mu_b}{\psi' - \psi_{cr}}\right)^4\right]^{-1/4} \left(\sqrt{\psi'} - 0.7\sqrt{\psi_{cr}}\right) \tag{62}$$

where

$$\psi' = \frac{(u'_*)^2}{(s-1)gd_{50}} = \frac{\tau_b{}'}{(s-1)\rho g d_{50}} \tag{63}$$

is the skin friction Shields parameter based on a skin friction roughness, $k_N = k'_N = 2.5d_{50}$, ψ_{cr} is the critical Shields parameter for incipient motion, and μ_b is a dynamic friction coefficient, which is recommended to be taken as unity by ZF94.

The values for the suspended-load transport, obtained in this manner, are then equated to the prediction afforded by *Einstein*'s [1950] suspended-load formula, i.e.

$$q_{S,ZF} = 11.6u'_* c_r z_r \left[I_1 \ln(\frac{30h}{2.5d_{50}}) + I_2\right] \tag{64}$$

where h is measured water depth, c_r is the reference concentration at a reference level $z_r = 2d_{50}$, I_1 and I_2 are Einstein's integrals, which are presented in graphical form in *Einstein* [1950] as functions of the dimensionless reference level z_r/h and the Rouse parameter

$$R = \frac{w_f}{\kappa u_*} \tag{65}$$

with the sediment fall velocity, w_f, obtained from *Rubey* [1933]

$$\frac{w_f}{\sqrt{(s-1)gd}} = \sqrt{\frac{2}{3} + \frac{36\nu^2}{gd^3(s-1)}} - \sqrt{\frac{36\nu^2}{gd^3(s-1)}} \tag{66}$$

and a value of u_* based on the total bottom shear stress, i.e. $k_N = k_m$ =movable bottom roughness. This shear velocity, u_*, is obtained from

$$u_* = \sqrt{ghS_0} \tag{67}$$

where S_0 is the (measured) channel slope. With

$$U = \frac{u_*}{\kappa} \ln \frac{11h}{k_m} = \frac{u_*{}'}{\kappa} \ln \frac{11h'}{k_N{}'} = \frac{u_*{}'}{\kappa} \ln \frac{11h'}{2.5d_{50}{}'} \tag{68}$$

where U is the (measured) cross-sectional average velocity, and

$$u_*' = \sqrt{gh'S_0} \tag{69}$$

Equation (68) can be solved for h' and the skin friction shear velocity, u_*', which represents the advective velocity, is obtained from equation (69).

With c_r being the only unknown, equation (64) is solved for c_r and the resulting values are represented by an empirical relationship for the reference concentration. Obviously, this relationship is a function of the procedures employed by ZF94 in their data analysis, e.g. their adoption of equation (62) as the bedload transport predictor influences the values obtained for c_r. Since the bedload transport formula by *Engelund and Fredsøe* [1976] has been found to underpredict the bedload transport rate, e.g. *Zhang and McConnachie* [1994], adopting a different bedload transport predictor might result in physically more realistic c_r-values. If we express the bedload transport rate q_{sB} predicted by our conceptual model presented in section 5.1 as

$$q_{sB} = (1 + \alpha_1) q_{B,ZF} \tag{70}$$

we obtain from equation (61) a suspended-load transport rate

$$q_{sS} = \left(1 - \frac{\alpha_1}{\alpha_2}\right) q_{S,ZF} = \gamma q_{S,ZF} \tag{71}$$

where:

$$\alpha_2 = \frac{q_{S,ZF}}{q_{B,ZF}} \tag{72}$$

Thus, the choice of an alternative bedload transport predictor simply modifies the suspended load transport rate by the factor

$$\gamma = 1 - \frac{\alpha_1}{\alpha_2} \tag{73}$$

and therefore simply results in changing the c_r-values obtained from equation (61) by a factor of γ. Thus, we obtain the following generalization of the reference concentration formula proposed by ZF94

$$c_r = \gamma \frac{0.331(\psi' - \psi_{cr})^{1.75}}{1 + 0.72(\psi' - \psi_{cr})^{1.75}} \tag{74}$$

where ψ_{cr} obtained from the Shields diagram replaces the constant value, 0.045, chosen for its simplicity by ZF94.

5.3.2. Application of ZF94 in unsteady oscillatory flows

Noting that we need to determine the maximum reference concentration, $c_{rm,0}$, in our model for suspended-load transport, we base our translation of the steady flow results, presented in section 5.3.1, to our unsteady oscillatory flow conditions when these are at or near their maximum values, which incidentally also corresponds to the time-interval when our flow is nearly steady.

From wave boundary layer analysis we obtain the maximum shear velocity from

$$\frac{\tau_{bm}}{\rho} = {u_{*m}}^2 = \frac{1}{2} f_w {U_{bm}}^2 \tag{75}$$

where f_w is given by equation (5) with $k_N = k_m$ =movable bed (or total) roughness. Many previous studies, e.g. *Dohmen-Janssen et al.* [2001], suggest that the presence of the sheet-flow layer leads to an increased total bottom shear stress, which can be characterized by an increased movable bed roughness, k_m. *Herrmann and Madsen* [2007] proposed a parametrization for k_m applicable to sheet-flow conditions, which can be generalized for sinusoidal oscillatory flows to read

$$k_m = [4.5 \cdot \max(0, \psi_m - \psi_{cr}) + 1.7]\, d_{50} \tag{76}$$

where ψ_m is a Shields parameter based on the maximum total bottom shear stress, i.e.

$$\psi_m = \frac{{u_{*m}}^2}{(s-1)gd} = \frac{f_w {U_{bm}}^2}{2(s-1)gd} \tag{77}$$

Since ψ_m is a function of k_m, the evaluation of k_m should be achieved by iteratively solving equations (5), (76) and (77). *Gonzalez-Rodriguez and Madsen* [2011] applied this total movable bottom roughness to model the boundary layer streaming under asymmetric oscillatory flows for sheet-flow conditions. Their successful predictions of experimentally observed streaming demonstrate that the total movable bed roughness by *Herrmann and Madsen* [2007] indeed leads to a good prediction of u_{*m}.

With u_{*m} known we can obtain an equivalent steady open channel flow of depth h_e by requiring that

$$U_{bm} = \frac{u_{*m}}{\kappa} \ln \frac{30 h_e}{k_m} \tag{78}$$

which is analogous to equation (68), and an equivalent slope

$$S_{0e} = \frac{{u_{*m}}^2}{g h_e} \tag{79}$$

obtained from equation (67). This equivalency concept is illustrated in Figure 9. The corresponding skin friction shear velocity, u'_{*m}, is then calculated from equation (68) and (69) with h_e and h'_e replacing h and h', and taking $S_0 = S_{0e}$. Alternatively, we may perform a wave boundary layer analysis for a bottom roughness $k_N = k'_N = 2.5d_{50}$ to obtain u'_{*m}. The two approaches lead, as seen from values listed in Table 6, to u'_{*m} predictions that differ by 1-2% for our experimental conditions.

With these equivalent steady open channel flow conditions the formulae and procedures employed by ZF94 and presented in section 5.3.1 are applicable. Because our bedload predictor, equation (29), differs from that chosen by ZF94, equation (62), we need the modification factor, γ, before the reference concentration specified at $z = z_r = 2d_{50}$ can be obtained from equation (74) with

$$\psi'_m = \frac{{u'_{*m}}^2}{(s-1)gd} \tag{80}$$

replacing ψ', i.e. we need a value for our bedload transport rate at maximum flow. This value, q_{sBm}, is obtained from equation (29) with $\tau_b(t) = \tau_{wmd}$, and the factor α_1 is obtained from equation (70) with $q_{sB} = q_{sBm}$ and $q_{B,ZF}$ evaluated from equation (62) for $\psi' = \psi'_m$. The factor α_2, defined by equation (72), is then obtained by computing $q_{S,ZF}$, equation (64), with u_*, u'_* and h replaced by u_{*m}, u'_{*m} and h_e, and c_r obtained from equation (74) with ψ'_m replacing ψ' and $\gamma = 1$. With α_1 and α_2 determined in this manner, γ is obtained from equation (73), and equation (74) yields a value of reference concentration specified $z = z_r = 2.5d_{50}$. Since our equivalent steady flow analogy is based on maximum unsteady flow condition, this value corresponds to the maximum reference concentration, i.e. precisely the $c_{rm,0}$ needed to determine the first harmonic concentration distribution in equation (58). Values of α_1, α_2, and γ for our experimental conditions are listed in Table 6. The obtained γ is less than one, because our bedload predictor yields a larger bedload transport rate than the choice of ZF94, i.e. the α_1-values are all positive.

With the reference concentration and the level where it is specified determined in this manner, the remaining parameters needed to evaluate our suspended-load model follow from the procedures employed by ZF94 in the analysis, i.e. (i) the shear velocity u_{*f}, needed to evaluate equation (48), is taken as u'_{*m} corresponding to a bottom roughness $k_N = k'_N = 2.5d_{50}$; (ii) the fall velocity, w_f, is obtained from *Rubey* [1933], equation (66), to be consistent with ZF94's choice; and (iii) the shear velocity scaling the turbulent diffusivity, u_{*D}, is taken as the shear velocity based on total (movable) bottom roughness, i.e. $u_{*D} = u_{*m}$ based on movable bottom roughness $k_N = k_m$ given by equation (76), to adhere to the procedures followed by ZF94. With these specifications of parameters, our model for suspended load sediment transport presented in section 5.2 is complete and truly predictive, i.e. it does not rely on any data-fitting.

5.4. Typical model prediction

Two tests, M1_S26 (medium sands) and F2_S26 (fine sands), with the same flow condition (U_{bm}=1.08 m/s, T=8.33 s) and bottom slope ($\beta = 2.60°$) are chosen as typical cases with negligible and significant sediment suspension, respectively. Figure 10 shows the predicted first-harmonic concentration and velocity for these two tests. The amplitude of the first-harmonic velocity follows the logarithmic profile in the very near bottom region and converges to the free-stream value at higher levels (z ∼100 mm), while the phase of the first-harmonic velocity increases from zero towards the bottom, leading to a 10-15° phase lead in the very near-bottom region. The amplitude of the first-harmonic concentration decreases rapidly with elevation z, as does its phase, e.g. the phase variation exceeds 100° across a depth of 100 mm. As a result, the phase difference between first-harmonic velocity and concentration changes dramatically from almost 180° in the immediate vicinity of the bottom to less than 90° at z=100 mm. The predicted net sediment flux shown in Figure 10e is therefore negative (downslope) in the very near-bottom region and decays drastically with elevation, leading to a net downslope suspended-load transport rate. The region with a significant net sediment flux is within z=10 mm for the medium-sand test, but can extend to about z=40 mm for the fine-sand test. Thus, the magnitude of net suspended sediment flux for the fine-sand test is much larger than that for the medium-sand test, so a much larger net downslope suspended-load transport is expected for the fine-sand test.

5.5. Model validation

Although our model can predict first-harmonic velocity and concentration, we shall not benchmark these predictions with experimental data, mainly because our model is only conceptual in the close vicinity of the movable bed, where most of the sediment transport occurs. The lack of suitable experimental data is another reason, e.g. the first-harmonic concentration is so small relative to the total concentration that it would be very difficult to make quantitative comparison with existing experimental data from other sources. Thus, in this section we only validate the prediction of net sediment transport rate against our measurements.

Since the predicted effect of bottom slope on instantaneous bedload transport rate is a factor of $1-\beta/\tan\phi_m$ ($\beta > 0$ for upslope) for a small bottom slope β, i.e. equation (28), a net downslope bedload transport rate scaled with β is expected for a sinusoidal flow over a sloping movable bed. Both the prediction of first-harmonic velocity and the normalized first-harmonic concentration are not functions of β, so the net suspended-load transport rate should be scaled by the amplitude of the first-harmonic reference concentration, which is also proportional to β, i.e. equation (39). These expectations are confirmed by predictions, so we can write the predicted non-dimensional total net transport rate as

$$q_{net,p} = -(\bar{q}_{sB} + \bar{q}_{sS}) = (A_b + A_s)\beta = A_p \cdot \beta \tag{81}$$

where A_p is the predicted slope, and A_b and A_s indicate the contribution from bedload and suspended-load transports, respectively. Introducing the minus sign is to make the predicted net transport rate positive in the downslope direction. The numerical values of A_p and the relative contributions from bedload and suspended-load, A_b/A_p and A_s/A_p, are shown in Table 7. The comparison between A_b/A_p and A_s/A_p suggests that bedload transport dominates for the coarse-sand test, whereas suspended-load transport dominates for fine-sand tests. Since the upward diffusion of sediments is characterized by the shear velocity u_{*D} and the tendency of sediment settling is characterized by the fall velocity w_f, the significance of suspended-load transport should increase with the ratio u_{*D}/w_f. The results in Table 7 show that the relative importance of suspended-load over bedload indeed increases with u_{*D}/w_f. The predicted suspended-load contributes more than 50% of the total transport for u_{*D}/w_f between 2.3 and 2.8 (the values for M1 and M2), which is in agreement with the threshold value for bedload to be dominant, $u_{*D}/w_f < 2.7$, proposed by *Gonzalez-Rodriguez and Madsen* [2007]. Our predictions for C1 and M1 seem to suggest that the relative importance of suspended load transport (A_s/A_p) dramatically increases for u_{*D}/w_f in the interval 2.1 to 2.3, as shown in Table 7. It should be noted that the net suspended transport rate is also controlled by other parameters, e.g. the skin friction Shields parameter (determines the reference concentration) and wave period (related to wave boundary layer thickness), so we cannot use u_{*D}/w_f as the sole indicator of the relative importance of suspended-load and bedload transports.

We showed a good linear $q_{net}-\beta$ dependency for measurements (Figure 5), so the model validation can be presented in terms of the slope A, i.e. A_p vs. A_m. As shown in Table 7, A_p is larger than A_m by roughly 60% for the bedload-dominated tests, e.g. C1, but is smaller than A_m by roughly 30% for the suspended-load-dominated tests, e.g. F1 and F2, indicating that the our model probably overestimates the net bedload transport rate, but underestimates the net suspended-load transport rate. The eddy diffusion for predicting sediment suspension is scaled by the maximum shear velocity, and it increases linearly with the distance from the bottom, while turbulence should vanish outside the wave boundary layer. Therefore, the eddy diffusion and hence the net suspended transport rate should be overestimated, which contradicts our results. *Yuan and Madsen* [2014] showed that for oscillatory flows in the WCS a secondary mean flow in the transverse plane is developed by sidewall effects, which can possibly enhance sediment suspension and increase the measured net suspended sediment transport rate. Visual evidence suggests that for fine-sand experiments sediments can be suspended outside the wave boundary layer, where no turbulence is expected to sustain suspension. It should also be pointed out that the vertical structure of the turbulent eddy viscosity and diffusivity will influence the prediction of the first-harmonic phase for both velocity and concentration, i.e. φ_{u1} and φ_{c1} in equation (42), which may have a significant effect on the prediction of net suspended-load transport rate. Nevertheless, the overall model accuracy is better than a factor of 2, and the overall agreement represented by the slope of the least-square fit to the data on A_p versus A_m plotted in Figure 11a is 1.04, suggesting a bias of a mere 4%, with a quite modest 95% confidence interval of ± 0.35. While this indicates the overall accuracy, it is more informative to look at the actual prediction of q_{net}. Figure 11b compares the predicted and the measured net sediment transport rates for all 30 tests in this study. Most of the predictions are within a factor of 2 from the measurements, and the overall agreement represented by the slope of the least-square fit to the data (thin dashed line in Figure 11a) is a factor of 1.03 with a 95% confidence interval of ± 0.12.

In the context of sediment transport modeling this performance, especially when considering that our predictive model was developed without use of the data against which its predictions were validated, is very encouraging and indicates that the underlying physics for net bedload and suspended-load transport rates are reasonably well captured by our model.

6. Conclusions

A full-scale (1:1) experimental study of bottom-slope-induced net sheet-flow sediment transport rates under sinusoidal oscillatory flows is conducted using an oscillatory water tunnel. Tests cover three sand sizes, six flow-sediment conditions and five bottom slopes from 0.1° to 2.6°. A laser-based bottom profiler system is developed to measure the bottom profile change over the entire 9-m long test section, so the net transport rate can be estimated based on the principle of sediment-volume conservation. Special attention is paid on the effect of flow-induced bed compaction, which is mitigated by applying a correction of bottom elevation change estimated from the difference between the LBP-measured volume loss of sands in the test section and the collected sand volume outside the test section.

For most tests a scour pit develops near the upslope end of the test section, while the downslope end exhibits either a smaller scour pit or a deposition hump. Around the longitudinal center of the test section, the bottom profile remains flat for the fine-sand tests, while for coarse-sand tests and some medium-sand tests long bedforms of very small steepness are observed to develop. These bedforms have little effect on the estimate of net transport rate, as evidenced by the fact that the net transport rate averaged over a few bedforms remains unchanged as the bedforms grow in height. The general discrepancy among repeated experiments is $\Delta q_{s,net} \sim O(1 \cdot 10^{-6}\ \mathrm{m}^2/\mathrm{s})$, which is much smaller than the measured net transport rate for most tests. Therefore, we conclude that the measurements are highly repeatable. This $\Delta q_{s,net}$, however, does not account for potential error in net transport rate from later inhomogeneity. By estimating the net sediment transport rate based on single laser lines, it is demonstrated that the effect of lateral inhomogeneity leads to an experimental inaccuracy in net transport rate of the order 10%-20% or less. Thus, the lateral inhomogeneity is the main source of experimental inaccuracy. Nevertheless, in the context of sediment transport, even a 20% error is considered quite acceptable. The measured net transport rate is always in the downslope direction, except for some tests on virtually horizontal bottoms ($\beta = 0.10°$). For a given flow-sediment condition the net transport rate exhibits near-perfect linear dependency on bottom slope, which agrees with the expectation based on a simple Taylor-series approximation.

A conceptual model is developed to interpret the experimental results. The net bedload sediment transport rate is obtained by period-averaging the instantaneous bedload transport rate predicted with the bedload transport model proposed by *Madsen* [1993], which conceptually accounts for the effect of bottom slope. The time series of the effective bottom shear stress for bedload transport is taken as the sum of first and third harmonics, which gives a maximum instantaneous bottom shear stress obtained from the wave boundary layer model by *Humbyrd* [2012] with the bottom roughness taken as the sediment diameter.

Assuming the near-bottom reference sediment concentration varies in concert with the instantaneous bedload transport rate in a quasi-steady manner, a non-zero bottom slope leads to a larger reference concentration when the flow is downslope than when it is upslope. This gives rise to a first-harmonic reference concentration, which is diffused upward into the water column. Based on Fourier-series representations, we identify that the net suspended-load transport rate is primarily due to the interaction between first-harmonic velocity and concentration. The analytical solution of the first-harmonic velocity is obtained following *Grant and Madsen* [1979]. The first-harmonic concentration is given by solving analytically the first-harmonic one-dimensional advection-diffusion equation with a first-harmonic reference concentration as the bottom boundary condition and an eddy diffusivity that is consistent with the eddy viscosity formulation used by *Grant and Madsen* [1979]. This reference concentration is obtained following *Zyserman and Fredsøe* [1994] with a modification based on a steady-unsteady-flow analogy to ensure model consistency. Also for consistency reason, our model parameters, e.g. the various bottom roughness specifications, are chosen corresponding to those employed in ZF94.

The predicted net bedload and suspended-load transport rates both increase linearly with bottom slope for a given flow-sediment condition. Comparing the predicted and measured gradients for the linear relationship between total transport rate and bottom slope, it is shown that the model predictions are equal to measurements within a factor of 2. The acceptable model accuracy allows us to interpret the key physics for the net downslope transport rate as follows. The bottom-parallel component of gravity helps the bottom shear stress to mobilize sand grains in the downslope direction, but hinders mobilization in the upslope direction. Thus, more sand grains are moving as bedload transport when the flow is in the downslope direction, leading to a net downslope bedload transport rate. The quantity of bottom sands available for suspension, which determines the reference concentration, is scaled by the amount of sand moving as bedload. Thus, a higher instantaneous reference concentration during downslope than during upslope transport is expected. This asymmetry can be represented by a first-harmonic reference concentration. In the very near-bottom region, the first-harmonic velocity and concentration are roughly 180° out of phase, leading to a net downslope suspended-load transport rate. Our prediction suggests that the relative importance of bedload and suspended-load transports depends on sediment diameter and flow condition. This simple model is a first attempt to quantitatively interpret slope-induced net sediment transport in the sheet-flow regime under oscillatory flows, so improvements to our predictive conceptual model should be explored in the future, e.g. adopting more realistic turbulent diffusivities including removal of the present model's inconsistent use of different turbulent eddy diffusivities for momentum and sediment.

The net total transport rate for tests on the 2.60° slope is comparable to the net transport rates due to flow skewness obtained in similar OWT sheet-flow studies. This suggests that bottom slope can be of equal importance to wave nonlinearity in producing a net sediment transport rate, and should be incorporated in modeling net cross-shore sediment transport rates. Future research effort is required to quantitatively elaborate the importance of bottom-slope effect.

Acknowledgments. This research is supported by the National Research Foundation (NRF), Prime Minister's Office, Singapore under its Campus for Research Excellence and Technological Enterprise (CREATE) programme. The Center for Environmental Sensing and Modeling (CENSAM) is an interdisciplinary research group (IRG) of the Singapore MIT Alliance for Research and Technology (SMART) centre. The author, Jing Yuan, also acknowledges the financial support from the Open Research Fund Program of State Key Laboratory of Hydroscience and Engineering of Tsinghua University. The key numerical information, e.g. net transport rate, is provided in the tables and figures in the paper. For detailed measurements, e.g. the raw data on bottom profile change, which are not included in tables, please contact the corresponding author (ceeyuan@nus.edu.sg).

References

Abramowitz, M., and I. A. Stegun (1965), *Handbook of mathematical functions*, Dover Publications.

Amoudry, L., T. J. Hsu, and P. L. F. Liu (2008), Two-phase model for sand transport in sheet flow regime, *Journal of Geophysical Research: Oceans*, *113*(C3), C03011, doi: 10.1029/2007JC004179.

Amoudry, L. O. (2012), Assessing sediment stress closures in two-phase sheet flow models, *Advances in Water Resources*, *48*, 92–101, doi: http://dx.doi.org/10.1016/j.advwatres.2012.03.011.

Asano, T. (1992), Two-phase flow model on oscillatory sheet-flow, *Proceedings of the 22nd International Conference on Coastal Engineering*, vol. 22, pp. 2372–2384, ASCE.

Davies, A. G., R. L. Soulsby, and H. L. King (1988), A numerical model of the combined wave and current bottom boundary layer, *J. Geophys. Res.*, *93*(C1), 491–508, doi: 10.1029/JC093iC01p00491.

Dohmen-Janssen, C., W. Hassan, and J. Ribberink (2001), Mobile-bed effects in oscillatory sheet flow, *Journal of Geophysical Research*, *106*(C11), 27103–27115, doi: 10.1029/2000JC000513.

Dong, L., S. Sato, and H. Liu (2013), A sheetflow sediment transport model for skewed-asymmetric waves combined with strong opposite currents, *Coastal Engineering*, *71*, 87–101, doi:http://dx.doi.org/10.1016/j.coastaleng.2012.08.004.

Einstein, H. A. (1950), The bed-load function for sediment transportation in open channel flows. technical bulletin no.1026, U.S. Dept. of Agr. Washingdon, D.C..

Engelund, F., and J. Fredsøe (1976), A sediment transport model for straight alluvial channels, *Nordic Hydrology*, *7*(5), 293–306.

Fetter, C. W. (2000), *Applied hydrogeology, 4th ed.*, Prentice hall, Inc.

Fuhrman, D. R., S. Schler, and J. Sterner (2013), Rans-based simulation of turbulent wave boundary layer and sheet-flow sediment transport processes, *Coastal Engineering*, *73*, 151–166, doi:http://dx.doi.org/10.1016/j.coastaleng.2012.11.001.

Gonzalez-Rodriguez, D., and O. S. Madsen (2007), Seabed shear stress and bedload transport due to asymmetric and skewed waves, *Coastal Engineering*, *54*(12), 914–929, doi: 10.1016/j.coastaleng.2007.06.004.

Gonzalez-Rodriguez, D., and O. S. Madsen (2011), Boundary-layer hydrodynamics and bedload sediment transport in oscillating water tunnels, *Journal of Fluid Mechanics*, *667*, 48–84, doi:10.1017/S0022112010004337.

Grant, W. D., and O. S. Madsen (1979), Combined wave and current interaction with a rough bottom, *Journal of Geophysical Research: Oceans*, *84*(C4), 1797–1808, doi: 10.1029/JC084iC04p01797.

Hassan, W. N., and J. S. Ribberink (2005), Transport processes of uniform and mixed sands in oscillatory sheet flow, *Coastal Engineering*, *52*(9), 745–770, doi: http://dx.doi.org/10.1016/j.coastaleng.2005.06.002.

Herrmann, M., and O. S. Madsen (2007), Effect of stratification due to suspended sand on velocity and concentration distribution in unidirectional flows, *Journal of Geophysical Research*, *112*(C02006), doi:10.1029/2006JC003569.

Holmedal, L. E., D. Myrhaug, and H. Rue (2003), The sea bed boundary layer under random waves plus current, *Continental Shelf Research*, *23*(7), 717–750, doi:10.1016/s0278-4343(03)00020-7.

Humbyrd, C. J. (2012), Turbulent combined wave-current boundary layer model for application in coastal waters, Master's thesis, Massachusetts Institute of Technology, Cambridge, MA, U.S.

King, D. B. (1991), Studies in oscillatory flow bedload sediment transport, Ph.D. thesis, University of California, San Diego, CA, U.S.

Kranenburg, W. M., J. S. Ribberink, J. J. L. M. Schretlen, and R. E. Uittenbogaard (2013), Sand transport beneath waves: The role of progressive wave streaming and other free surface effects, *Journal of Geophysical Research: Earth Surface*, *118*(1), 122–139, doi:10.1029/2012JF002427.

Li, M., S. Pan, and B. A. O'Connor (2008), A two-phase numerical model for sediment transport prediction under oscillatory sheet flows, *Coastal Engineering*, *55*(12), 1159–

1173, doi:http://dx.doi.org/10.1016/j.coastaleng.2008.05.003.

Longuet-Higgins, M. S. (1953), Mass transport in water waves, *Philosophical Transactions of the Royal Society of London. Series A, Mathematical and Physical Sciences*, *245*(903), 535–581.

Madsen, O. S. (1991), Mechanics of cohesionless sediment transport in coastal waters, *Proceedings of Coastal Sediments '91.*, pp. 1527, ASCE.

Madsen, O. S. (1993), *Sediment transport outside the surf zone*, Technical Report U.S. Army Engineer Waterways Experiment Station.

Madsen, O. S. (2002), *Sedment transport outside the surf zone*, Coastal Engineering Manual, vol. III. U.S. Army Corps of Engineers, Washington DC. Chapter 6.

Madsen, O. S., and W. D. Grant (1976), Quantitative description of sediment transport by waves, *Proceedings of the 15th International Conference on Coastal Engineering*, vol. 2, pp. 1093–1112, ASCE.

McLean, S. R., J. S. Ribberink, C. M. Dohmen-Janssen, and W. N. Hassan (2001), Sand transport in osciliatory sheet flow with mean current, *Journal of Waterway, Port, Coastal, and Ocean Engineering*, *127*(3), 141–151, doi:10.1061/(ASCE)0733-950X(2001)127:3(141).

O'Donoghue, T., and S. Wright (2004), Flow tunnel measurements of velocities and sand flux in oscillatory sheet flow for well-sorted and graded sands, *Coastal Engineering*, *51*(11-12), 1163–1184, doi: http://dx.doi.org/10.1016/j.coastaleng.2004.08.001.

Ribberink, J., and A. Al-Salem (1994), Sediment transport in oscillatory boundary layers in cases of rippled beds and sheet flow, *Journal of Geophysical Research*, *99*(C6), 12707–12727, doi:10.1029/94JC00380.

Ribberink, J., and A. Al-Salem (1995), Sheet flow and suspension of sand in oscillatory boundary layers, *Coastal Engineering*, *25*(3-4), 205–225, doi:10.1016/0378-3839(95)00003-T.

Rubey, W. (1933), Settling velocity of gravel, sand, and silt particles, *American Journal of Science*, *25*(5), 325–338.

Ruessink, B. G., T. J. J. van den Berg, and L. C. van Rijn (2009), Modeling sediment transport beneath skewed asymmetric waves above a plane bed, *Journal of Geophysical Research: Oceans*, *114*(C11), 1-14, doi:10.1029/2009JC005416.

Ruessink, B. G., H. Michallet, T. Abreu, F. Sancho, D. A. van der A, J. J. van der Werf, and P. A. Silva (2011), Observations of velocities, sand concentrations, and fluxes under velocity-asymmetric oscillatory flows, *Journal of Geophysical Research*, *116*(C3), C03004.

Trowbridge, J., and O. S. Madsen (1984), Turbulent wave boundary layers: 2. second-order theory and mass transport, *Journal of Geophysical Research: Oceans*, *89*(C5), 7999–8007, doi:10.1029/JC089iC05p07999.

van der A, D. A., T. O'Donoghue, and J. S. Ribberink (2010), Measurements of sheet flow transport in acceleration-skewed oscillatory flow and comparison with practical formulations, *Coastal Engineering*, *57*(3), 331–342. doi: http://dx.doi.org/10.1016/j.coastaleng.2009.11.006

van der A, D. A., T. O'Donoghue, A. Davies, and J. S. Ribberink (2011), Experimental study of the turbulent boundary layer in acceleration-skewed oscillatory flow, *Journal of Fluid Mechanics*, *684*, 251–283. doi:DOI: http://dx.doi.org/10.1017/jfm.2011.300

van der Werf, J., J. Doucette, T. O'Donoghue, and J. S. Ribberink (2007), Detailed measurements of velocities and suspended sand concentrations over full-scale ripples in regular oscillatory flow, *Journal of Geophysical Research*, *112*, F02012, doi: 10.1029/2006JF000614.

Wikramanayake, P. N. (1993), Velocity profiles and suspended sediment transport in wave-current flows, Ph.D. thesis, Massachusetts Institute of Technology, Cambridge, MA, U.S.

Yuan, J., and O. S. Madsen (2014), Experimental study of turbulent oscillatory boundary layers in an oscillatory water tunnel, *Coastal Engineering*, *89*, 63–84, doi: http://dx.doi.org/10.1016/j.coastaleng.2014.03.007

Zhang, X., and G. L. McConnachie (1994), A reappraisal of the Engelund bed load equation, *Hydrological Sciences Journal*, *39*(6), 561–567,doi:10.1080/02626669409492780

Zyserman, J., and Fredsøe (1994), Data analysis of bed concentration of suspended sediment, *Journal of Hydraulic Engineering*, *120*(9), 121–1042, doi:10.1061/(ASCE)0733-9429(1994)120:9(1021).

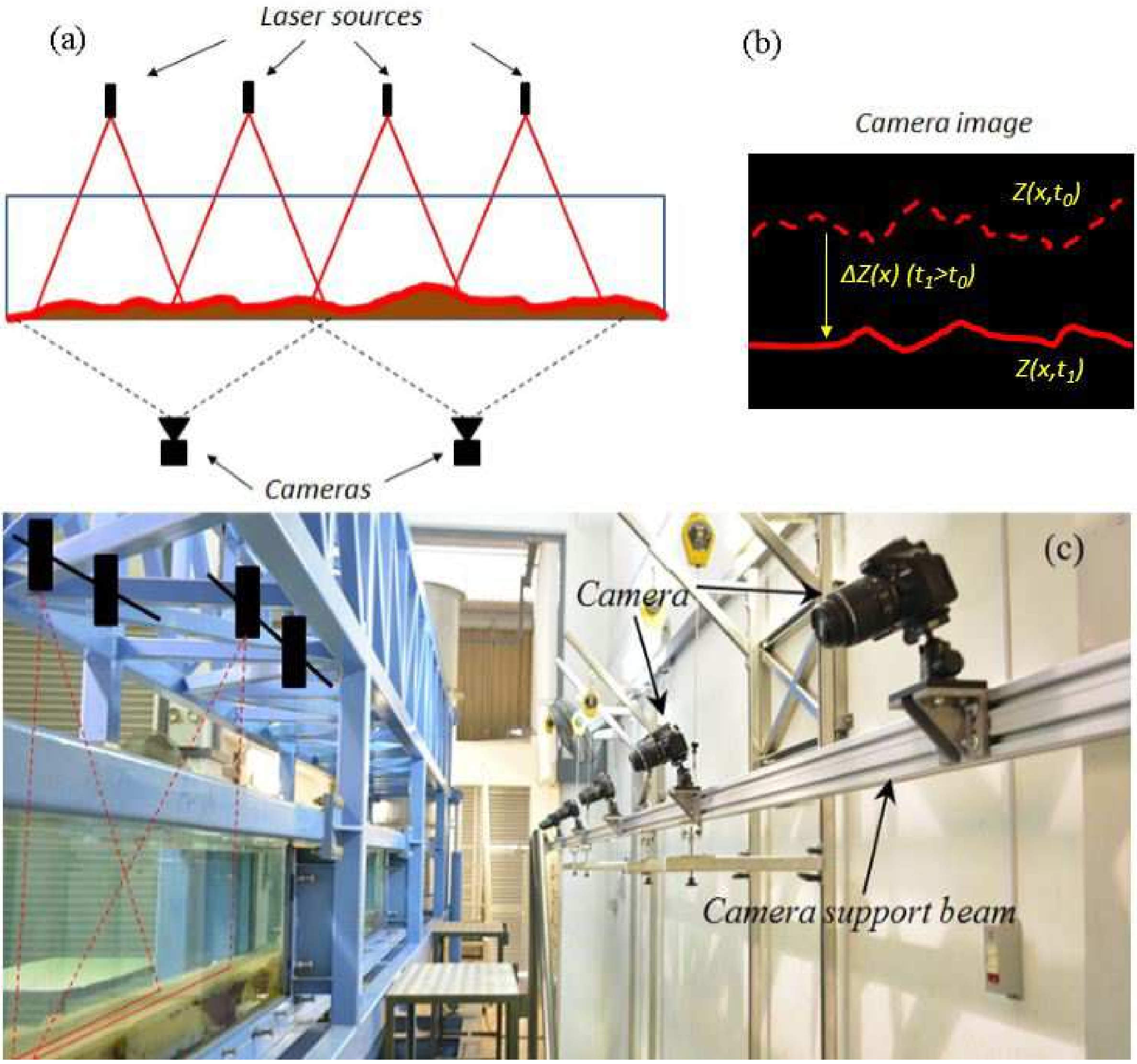

Figure 1. The Laser-based Bottom Profiler (LBP) system: (a) general concept of LBP, (b) illustration of the vertical movement of a laser line on a camera image, (c) system setup (the test section of WCS is 10m-long, 40cm-wide and 50cm-deep).

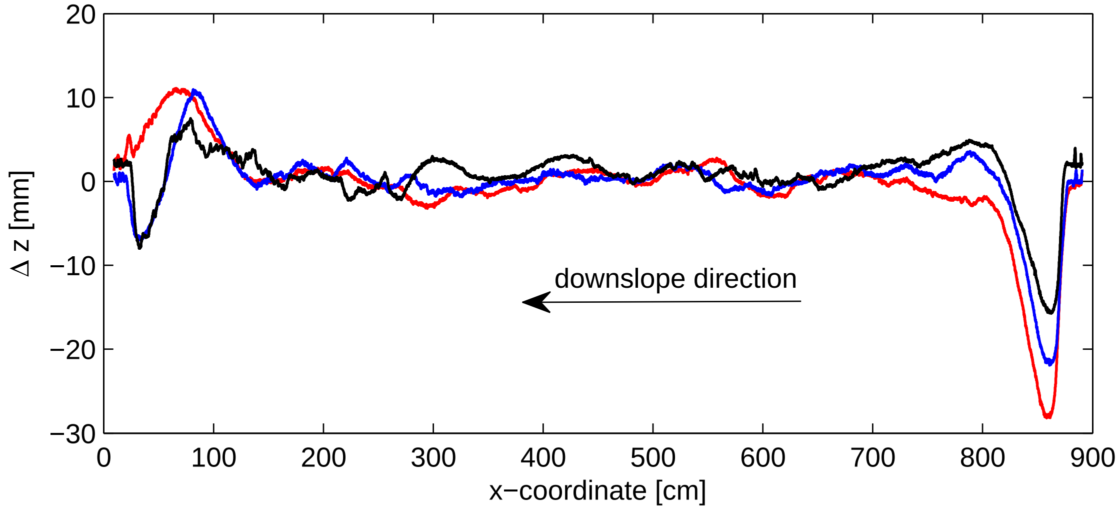

Figure 2. Typical observations of bottom profile change Δz after one test (red line: F1_S26, blue line: test F1_S11, black line: test F1_S01)

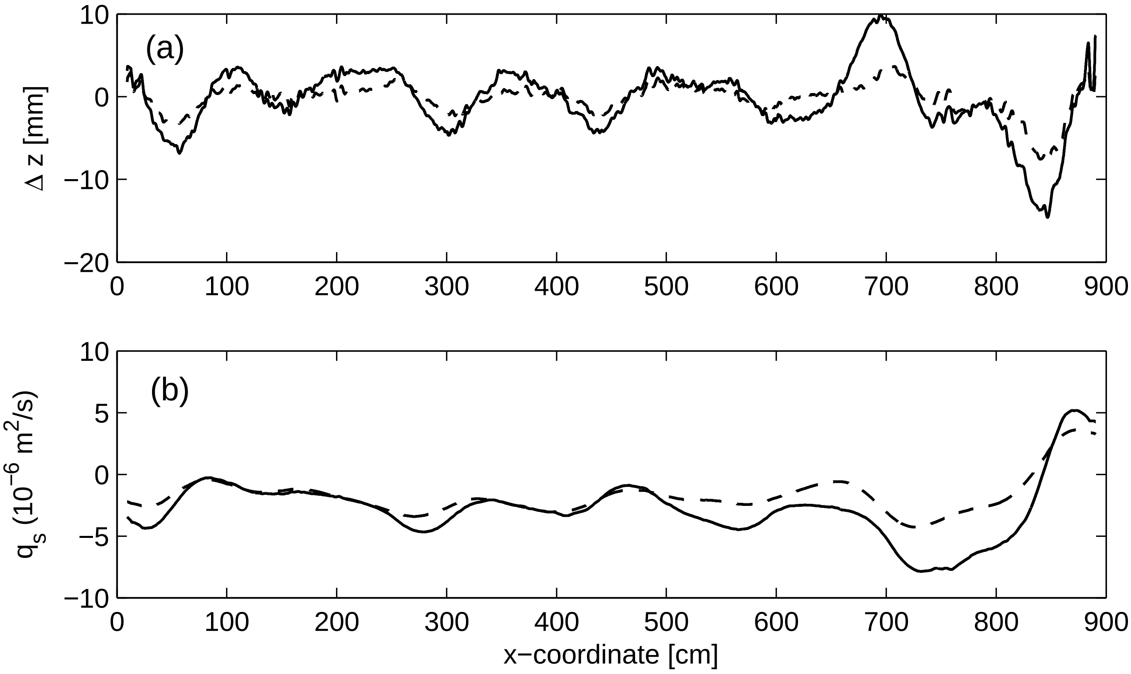

Figure 3. Development of bedforms for a medium-sand test M2_S06 and the associated effect on net transport rate (full lines: after 50 periods, dashed lines: after 25 periods): (a) bottom elevation change ≈ bottom profile, (b) variation of net transport rate along the test section

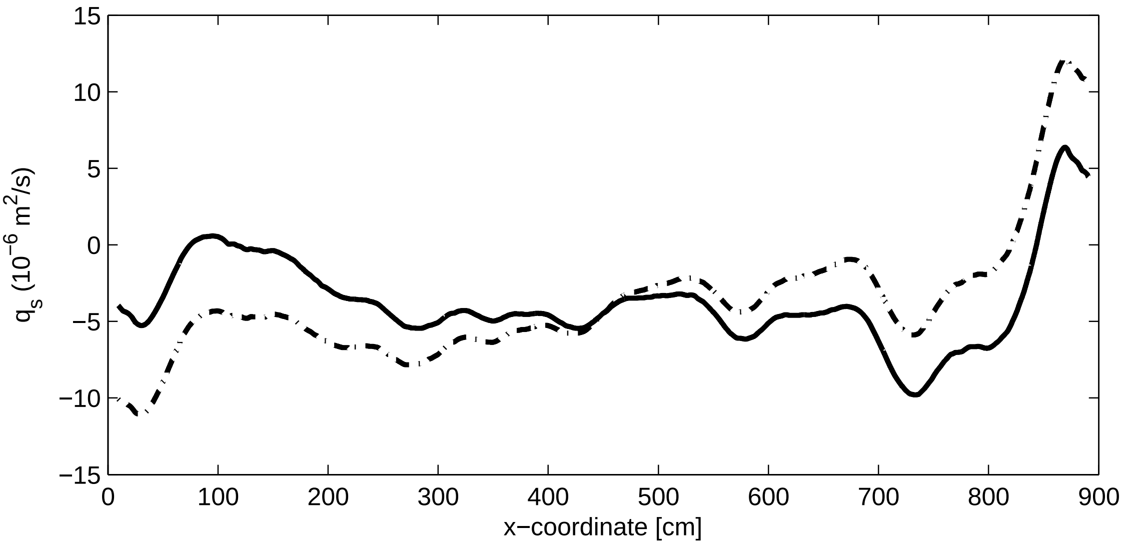

Figure 4. Experimental obtained variation of net transport rate q_s over the entire test section for a typical test M2_S11 (solid line: bed-compaction correction, dash-dotted line: simple-average correction).

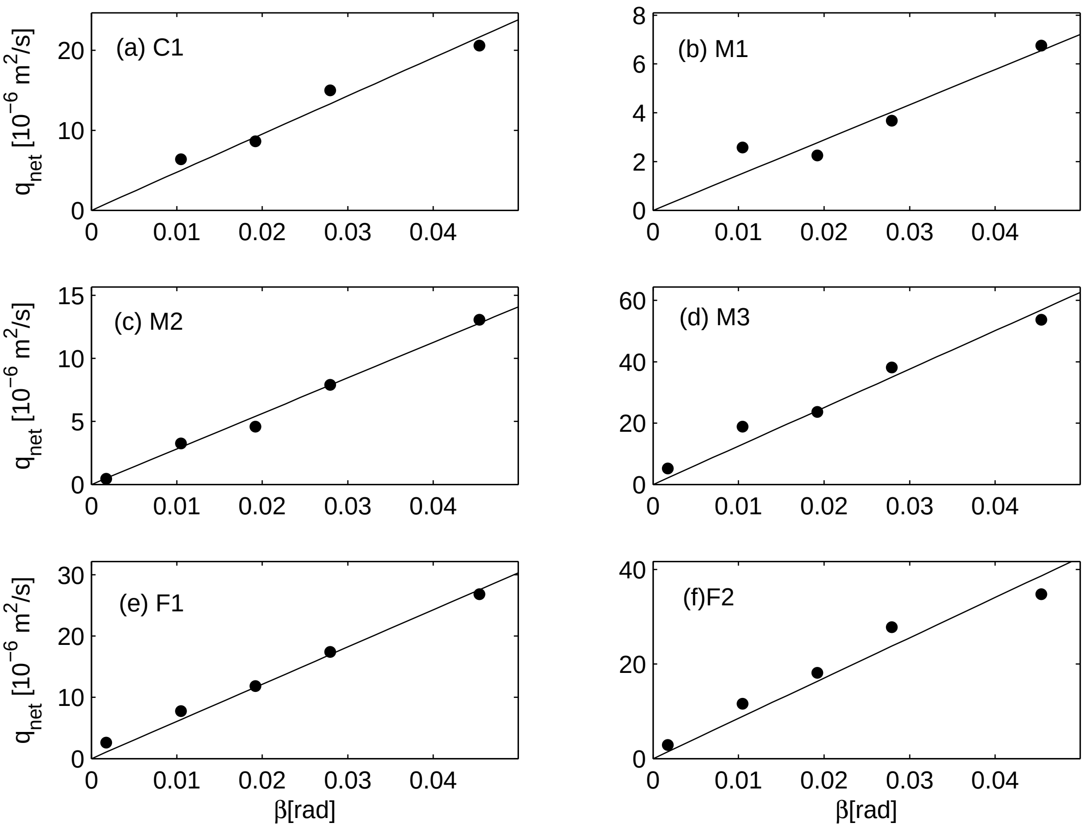

Figure 5. Variation of net transport rate with bottom slope for a given flow-sediment condition. For C1 and M1, measured q_{net} for 0.1°-tests (or 0.0017 [rad]) are negative (up-slope net transport rate) but negligibly small (comparable to measurement accuracy), so the results are not shown. (solid lines: fitted linear function $q_{net} = A\beta$ (details are presented in Table4), full circles: measurements).

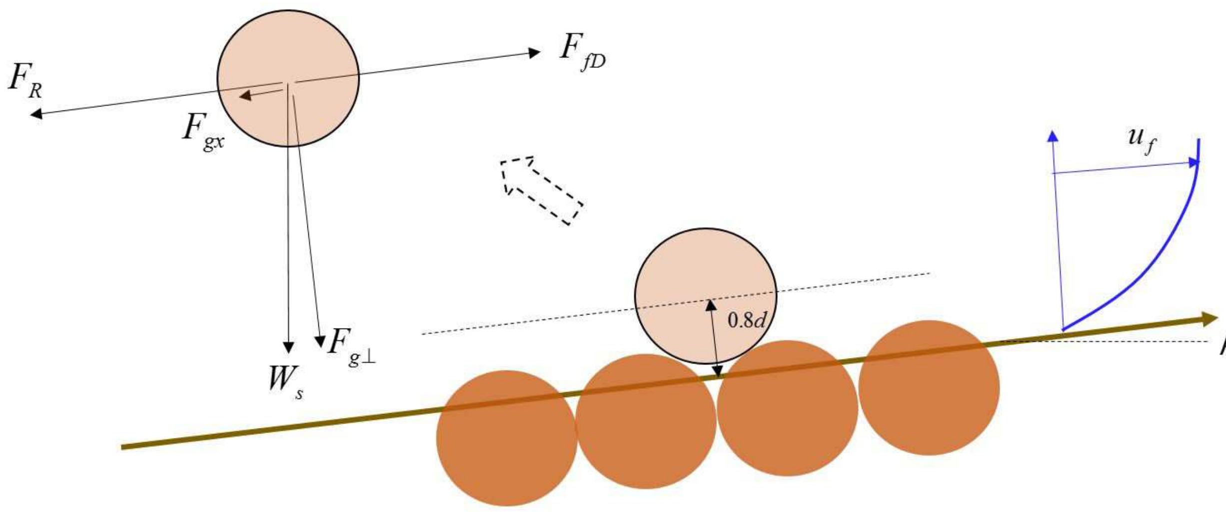

Figure 6. Forces acting on a spherical sediment grain resting or moving on a plane bed

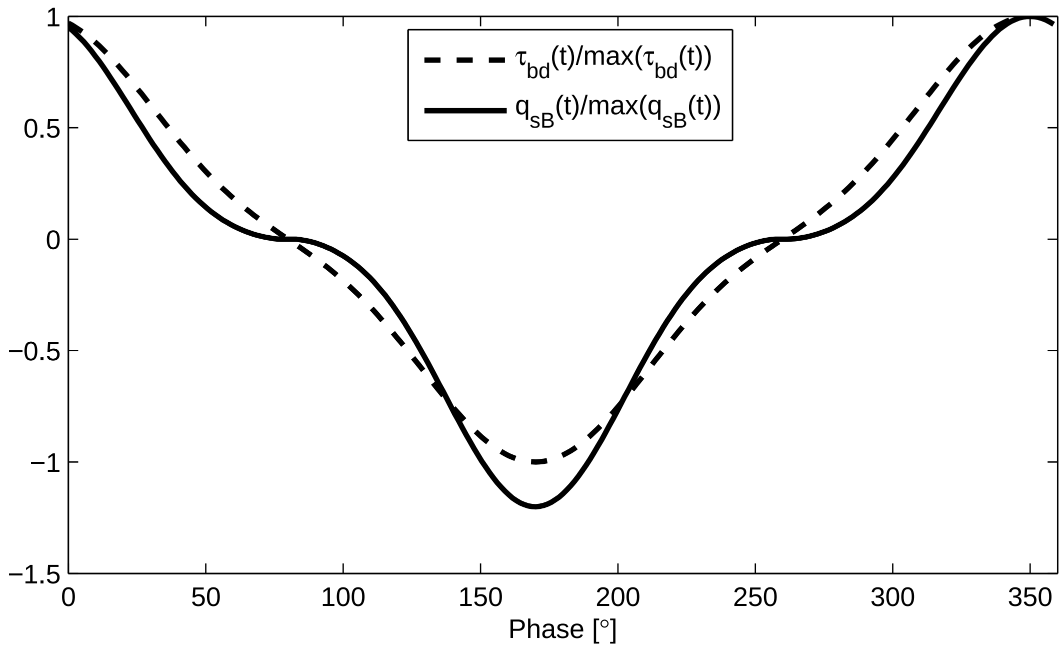

Figure 7. Normalized effective bottom shear stress (dashed line) and instantaneous bedload transport rate (solid line) for test M3_S26 (the maximum effective bottom shear stress is 7.7 pa, and maximum upslope bedload transport rate is $5.1 \cdot 10^{-4} m^2$/s. The negative direction is downslope).

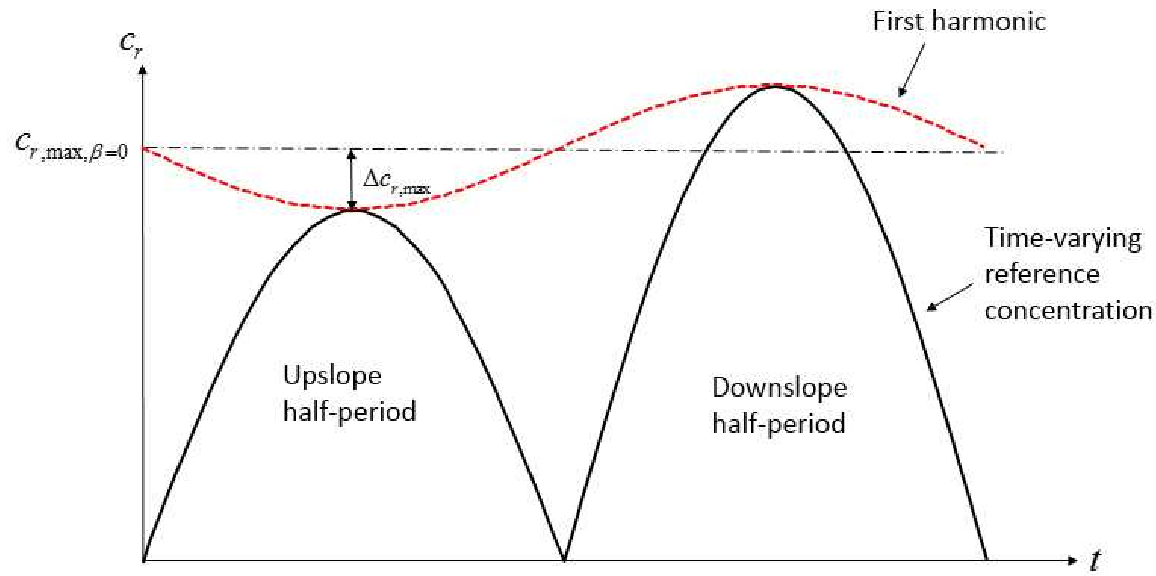

Figure 8. Illustrative drawing of the temporal variation of reference concentration under the influence of bottom slope

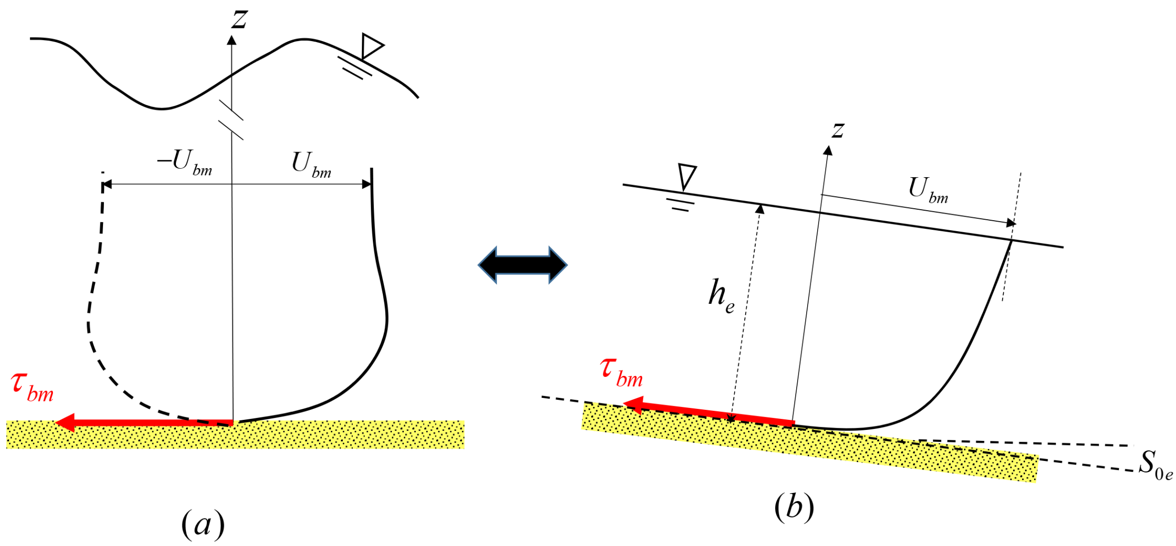

Figure 9. Illustrative drawing for the steady-flow analogy: (a) wave boundary layer flow at maximum flow condition, (b) equivalent steady flow

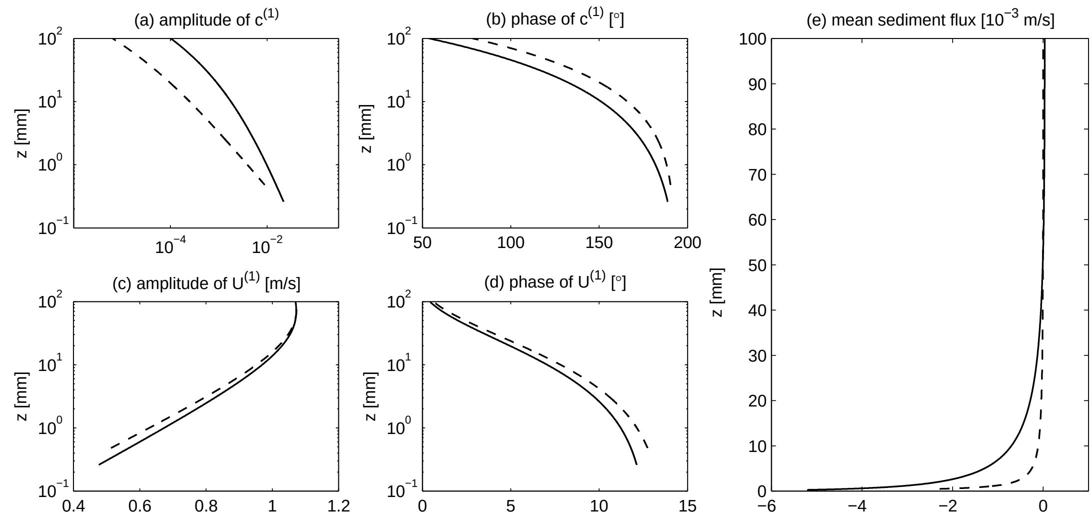

Figure 10. Prediction of first-harmonic velocity and concentration for tests M1_S26 (dashed lines) and F2_S26 (solid lines): (a) amplitude of first-harmonic concentration, (b) phase of first-harmonic concentration, (c) amplitude of first-harmonic velocity, (d) phase of first-harmonic velocity, (e)net Sediment flux (the negative direction is downslope).

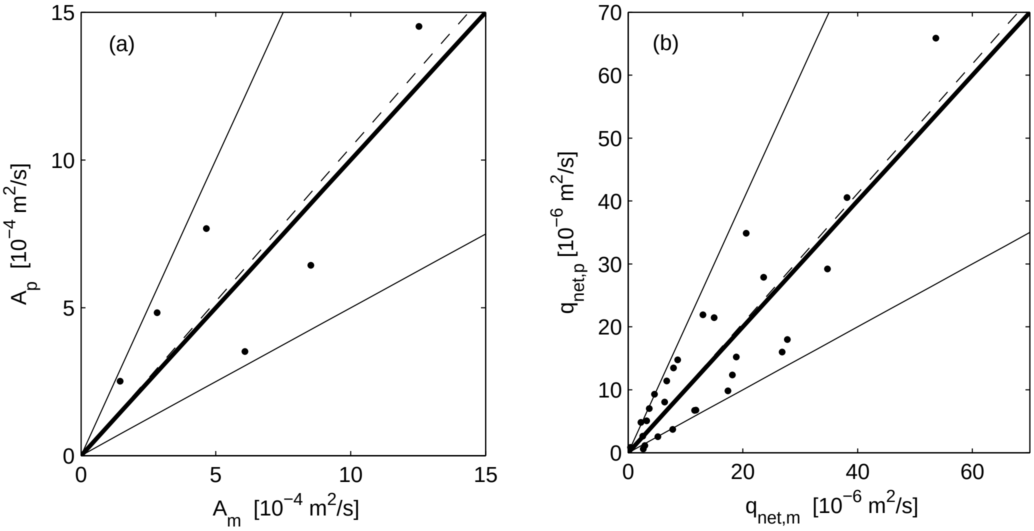

Figure 11. Model validation: (a) comparison of predicted (A_p) and measured (A_m) slopes for the linear relationship between net sediment transport rate and bottom slope for the different flow-sediment conditions (the heavy solid line indicates perfect agreement; the thin solid lines indicate a factor of 2 deviation from perfect agreement; the dashed line is the best fit through origin (slope is 1.04 with a 95% confidence interval of 0.35)).(b) comparison of predicted ($q_{net,p}$) and measured ($q_{net,m}$) net sediment transport rate (the solid lines are as in (a); the dashed line is the best fit through origin (slope is 1.03 with a 95% confidence interval of 0.12)

Table 1. Sediment characteristics. [a]

Type	d_{50}(mm)	σ_g	s	ϵ_m
Fine sand	0.13	1.38	2.650±0.004	0.436±0.0004
Medium sand	0.24	1.37	2.651±0.003	0.424±0.0011
Coarse sand	0.51	1.43	2.628±0.013	0.482±0.0023

[a] d_{50} is the medium diameter of sediments, σ_g is the geometric standard deviation, s is specific particle density and ϵ_m is the maximum underwater porosity.

Table 2. Summary of tests. [a]

Test ID	U_{bm}(m/s)	T(s)	d_{50}(mm)	ψ_{wmd}	slope(°)	Repeats	$q_{s,net}$(10^{-6}m^2/s)	$\Delta q_{s,net}$(10^{-6}m^2/s)
C1_S01	1.61	6.25	0.51	1.13	0.1	1	1.1	
C1_S06	1.61	6.25	0.51	1.13	0.6	2	-6.4	0.3
C1_S11	1.61	6.25	0.51	1.13	1.1	1	-8.6	
C1_S16	1.61	6.25	0.51	1.13	1.6	1	-15.0	
C1_S26	1.61	6.25	0.51	1.13	2.6	2	-20.6	0.2
M1_S01	1.06	8.33	0.24	0.89	0.1	1	0.0	
M1_S06	1.06	8.33	0.24	0.89	0.6	1	-2.6	
M1_S11	1.06	8.33	0.24	0.89	1.1	1	-2.3	
M1_S16	1.06	8.33	0.24	0.89	1.6	1	-3.7	
M1_S26	1.06	8.33	0.24	0.89	2.6	1	-6.8	
M2_S01	1.21	6.25	0.24	1.20	0.1	2	-0.5	0.3
M2_S06	1.21	6.25	0.24	1.20	0.6	2	-3.3	0.5
M2_S11	1.21	6.25	0.24	1.20	1.1	1	-4.6	
M2_S16	1.21	6.25	0.24	1.20	1.6	1	-7.9	
M2_S26	1.21	6.25	0.24	1.20	2.6	4	-13.1	0.6
M3_S01	1.61	6.25	0.24	2.00	0.1	1	-5.2	
M3_S06	1.61	6.25	0.24	2.00	0.6	1	-18.9	
M3_S11	1.61	6.25	0.24	2.00	1.1	1	-23.6	
M3_S16	1.61	6.25	0.24	2.00	1.6	1	-38.2	
M3_S26	1.61	6.25	0.24	2.00	2.6	1	-53.7	
F1_S01	0.90	4.17	0.13	1.27	0.1	1	-2.6	
F1_S06	0.90	4.17	0.13	1.27	0.6	2	-7.8	0.8
F1_S11	0.90	4.17	0.13	1.27	1.1	1	-11.8	
F1_S16	0.90	4.17	0.13	1.27	1.6	2	-17.4	0.2
F1_S26	0.90	4.17	0.13	1.27	2.6	1	-26.8	
F2_S01	1.06	8.33	0.13	1.43	0.1	2	-2.9	1.3
F2_S06	1.06	8.33	0.13	1.43	0.6	1	-11.6	
F2_S11	1.06	8.33	0.13	1.43	1.1	1	-18.2	
F2_S16	1.06	8.33	0.13	1.43	1.6	2	-27.8	2.6
F2_S26	1.06	8.33	0.13	1.43	2.6	2	-34.7	3.4

[a] U_{bm} and T are the amplitude and period of free-stream velocity, respectively, ψ_{wmd} is the Shields parameter based on $k_N = d_{50}$, d_{50} is the median sediment diameter, $q_{s,net}$ is the compaction-corrected experimental net transport rates (positive in the upslope direction) and $\Delta q_{s,net}$ is half the difference between two repeats (or the standard deviation for more than two repeats).

Table 3. Comparisons between tests with or without re-working the initial movable bed.

	δz (mm)		$q_{s,net}$ (10^{-6} m^2/s)	
	1st test	2nd test	1st test	2nd test
M2_S01	0.255	0.125	-0.12	-0.79
M2_S06	0.147	0.090	-2.78	-3.72
M2_S26	0.152	0.048	-12.80	-13.10

Table 4. Results for linear-function fitting of $q_{net} = A \cdot \beta$, as shown in Figure5. [a]

Test	U_{bm}(m/s)	T (s)	d_{50}(mm)	A(±%) (10^{-4} m^2/s)	R^2
C1	1.61	6.25	0.51	4.65 (14%)	0.97
M1	1.06	8.33	0.24	1.45 (22%)	0.93
M2	1.21	6.25	0.24	2.83 (8%)	0.99
M3	1.61	6.25	0.24	12.53 (15%)	0.95
F1	0.90	4.17	0.13	6.08 (9%)	0.98
F2	1.61	8.33	0.13	8.52 (18%)	0.93

[a] U_{bm} and T are the amplitude and period of free-stream velocity, respectively, d_{50} is the sediment diameter, A is the fitted slope (the percentage in the following bracket indicates the relative 95% confidence limits). R^2 is the coefficient of determination.

Table 5. Effect of lateral inhomogeneity on the slope of linear relationship, $q_{net} = A \cdot \beta$, between net transport rate and bottom slope for a given flow sediment condition (the percentage in the brackets indicate relative 95% confidence limits). [a]

	C1	M1	M2	M3	F1	F2
A_1 [10^{-4}m^2/s]	4.23 (17%)	1.60 (53%)	3.38 (14%)	13.88 (29%)	6.20 (8%)	8.33 (9%)
A_2 [10^{-4}m^2/s]	5.20 (23%)	1.29 (23%)	2.33 (23%)	11.16 (32%)	5.95 (11%)	8.73 (12%)
A [10^{-4}m^2/s]	4.65 (14%)	1.45 (22%)	2.83 (8%)	12.53 (15%)	6.08 (9%)	8.52 (18%)
$\lvert A1 - A2\rvert/(2A)$ [%]	10.4	10.8	18.6	10.9	2.0	2.3

[a] A is the slope for the net transport rate based on the averaged bottom profile change Δz, while A_1 and A_2 are slopes for the net transport rate based on single laser lines. $|A1 - A2|/(2A)$ indicates the deviation of A_1 and A_2 from A.

Table 6. Modification of ZF94 reference concentration based on steady-flow analogy.[a]

ID	Wave boundary layer			Equivalent steady flow			Transport rate			
	u_{*m} $[cm/s]$	$\frac{k_m}{d_{50}}$	u'_{*m} $[cm/s]$	h_e $[cm]$	S_{0e} $[10^{-2}]$	u'_{*m} $[cm/s]$	$q_{B,ZF}$ $[10^{-5}m^2/s]$	α_1	α_2	γ
C1	13.9	12.0	10.9	2.12	9.2	11.1	25	1.8	2.2	0.18
M1	7.8	8.6	6.6	1.51	4.1	6.7	6.9	1.2	2.4	0.50
M2	9.7	12.4	7.7	1.44	6.6	7.8	8.3	2.0	4.4	0.55
M3	13.6	23.0	9.9	2.07	9.1	10.1	11	4.0	12.5	0.68
F1	7.4	13.2	5.8	0.74	7.6	5.9	3.3	2.1	10.4	0.80
F2	7.7	14.1	6.1	1.48	4.1	6.2	3.5	2.6	19.0	0.87

[a] see section 5.3 for definition of variables

Table 7. Model validation in terms of the slope A in $q_{net} = A \cdot \beta$.

ID	U_{bm}(m/s)	T(s)	u_{*D}/w_f	A_m	A_p	A_b/A_p	A_s/A_p
C1	1.61	6.25	2.1	4.65	7.68	82.0%	18.0%
M1	1.06	8.33	2.3	1.45	2.51	54.8%	45.2%
M2	1.21	6.25	2.8	2.83	4.83	46.1%	53.9%
M3	1.61	6.25	3.9	12.53	14.52	33.8%	66.2%
F1	0.90	4.17	4.7	6.08	3.52	26.4%	73.6%
F2	1.06	8.33	4.9	8.52	6.44	17.5%	82.5%

[a] the fall velocity w_f is predicted using *Rubey* [1933]'s formula. A_m and A_p are measurement and prediction, respectively. A_b and A_s are predictions for net bedload and suspended-load transport rates, respectively.